

INSTRUCTION MANUAL
COSMICWATCH
THE DESKTOP MUON DETECTOR (v3X)

Contacts:

Prof. Spencer Axani (saxani@udel.edu)
Masooma Sarfraz (masoomas@udel.edu)
Miles Garcia (milesg@udel.edu)

May 1, 2025

Contents

1 DOCUMENT OVERVIEW	4
2 SOURCES OF IONIZING RADIATION	6
2.1 Cosmic radiation	6
2.1.1 Flux variations due to solar system properties	10
2.1.2 Flux variations due to atmospheric properties	11
2.2 Radioactive backgrounds	12
3 PARTICLE INTERACTIONS WITH MATTER	14
3.1 High energy heavy charged particles	14
3.2 High energy electrons/positrons and photons	16
3.3 Low energy electrons/positrons	17
3.4 Low energy gamma rays	18
3.5 Neutrons	19
4 DETECTION METHODS	21
4.1 Single Photon Detection: Photomultipliers	21
4.2 Scintillators	23
5 THE COSMICWATCH DETECTOR	26
5.1 Introduction to the Detector	26
5.2 Setting detectors in coincidence mode	27
5.3 Recording data options	30
6 HOW TO BUILD A COSMICWATCH DETECTOR V3X	34
6.1 Overview	34
6.1.1 (1) Purchasing the components	34
6.1.2 Populating the PCBs	34
6.2 Taking your first data	41
6.3 Things you should understand	42
6.3.1 Discussion about backgrounds in a set of coincidence events	43
7 TESTED MEASUREMENTS YOU CAN CHOOSE FROM	46
7.1 Cosmic-ray Muon Angular Distribution	47

7.2	Cosmic-ray muon attenuation in a Subway station	48
7.3	Electromagnetic component of cosmic-ray showers	49
7.4	Reducing radioactive backgrounds	50
7.5	Correlation between the cosmic-ray muon rate and atmospheric pressure	51
7.6	A true random number generator?	53
7.7	Gamma-ray spectroscopy	56
8	UNTESTED MEASUREMENTS FOR THE ADVENTUROUS	57
8.1	The velocity of cosmic-ray muons	58
8.2	Muon Rate Underwater	59
8.3	Muon lifetime	60
8.4	Solar flares and the Forbush decrease	61
8.5	Measuring the air shower size	62
9	FUN MEASUREMENTS WE HAVE DONE	64
9.1	Measuring the cosmic-ray muon rate in an airplane at 33,000 ft	64
9.2	High altitude balloon measurement at 107,000 ft	65
9.3	Muon rate measurement while flying to the South Pole	67
9.4	Latitude correction to the cosmic-ray muons	69
9.5	Rate measurement 1 km underground at Super-Kamiokande	71
9.6	Portable trigger system for an accelerator beamline	73
10	FUTURE MEASUREMENTS	74
11	CONCLUSION	75
A	Detailed description of the electronics	76
A.1	The analog circuit	76
A.1.1	The amplifier	76
A.1.2	The peak detector	78
A.1.3	The comparator	78
A.2	Digital circuit	78
A.2.1	Raspberry Pi Pico	79
A.2.2	SD card writer	79
A.2.3	Temperature and pressure sensor	79
B	The Firmware	81

Chapter 1

DOCUMENT OVERVIEW

The CosmicWatch Detector v3X is a compact, self-contained, inexpensive (100\$), low-power (0.5 W), particle detector that uses a plastic scintillator and silicon photomultiplier to explore particle, nuclear, astro-, and geophysics. Through these detectors we can explore a wide range of phenomena, including muon energy loss in materials, special relativity, radioactive decay, cosmic ray shower composition, and much more. The detectors support standalone data logging to microSD or live USB streaming, offers coincidence mode for background suppression, and logs rich event metadata (e.g. timestamp, ADC value, temperature, pressure, acceleration). Fully open-source with detailed build instructions and provided Python analysis scripts, v3X will be useful for education, outreach, citizen science, and more advanced cosmic-ray studies.

This instruction manual provides a comprehensive exploration of the CosmicWatch Desktop Muon Detectors v3X. It starts by describing the sources of ionizing radiation that we need to consider for the remainder of the document. After that, we'll work through how each of these forms of radiation interact with materials and how the detectors measure their interaction. We'll then shift to details specific to the detectors, discussing the technology employed and provide instructions on how to build a detector yourself. The last few chapters of the document illustrates various physical phenomena discussed in earlier chapters through measurements conducted specifically with the detectors. As students generate new study ideas using this detector and analyze fresh data, these concluding chapters are envisioned to undergo continuous updates.

All material for v3X can be found in the GitHub repository located here:

<https://github.com/spenceraxani/CosmicWatch-Desktop-Muon-Detector-v3X>

Version v3X represents a significant advancement over the previous v2 detector. In addition to the significant improvements in the analog electronics, high-frequency PCB design, and component optimization, v3X delivers orders-of-magnitude enhancements across several performance metrics and also introduces new functionality, as illustrated in Fig. 1.1.

v2	Technical Spec.	v3X
ATmega328P	Processor	Arm Cortex-M0+
Single core	Number of Cores	Dual core
16 MHz clock	Clock Frequency	133 MHz clock
32KB	CPU memory	2MB
2KB	RAM	264KB
0.27W	Power consumption	0.5W
<8-bit	ADC resolution	12-bit
50 Hz	Max event rate	1,000 Hz
0.5 mV	Noise level [RMS]	0.1 mV
No	Wifi/Bluetooth (later)	Yes
No	GPS/RT clock (later)	Yes
Not at same time	OLED + SD	Yes
No	Accelerometer	Yes
No	Pressure monitor	Yes
Yes	Temperature monitor	Yes
No	Gamma-ray Spec.	Yes
25 cm ²	Effective area	25cm ²
50ms	Deadtime per event	60 µs
67 g	Weight	67 g
No	Citizen Science (later)	Yes
36 mm ²	Photocathode area	36mm ²
12 mV	Min trigger threshold	4mV
No	Records all events	Yes
450 µHz	Accidental coincident rate	< 54 µHz
100 USD	Cost	100 USD

Figure 1.1: A comparison between the v2 (previous version of the detector) and v3X.

Cosmic Rays and Particle Physics [6], proves to be extremely useful.

For a comprehensive understanding of energy loss in matter, *Techniques for Nuclear and Particle Physics* by W. Leo [7] stands out as one of the best resource for experimental particle physics. Additionally, Prof. C. Grupen's textbook, *Particle Detectors* [8] and *Particle Detectors: Fundamentals and Applications* [9] by H. Kolanoski, are extremely highly recommended as a reference for describing detection methods in particle physics.

Components of this instructions manual has been lightly adapted from MIT's Junior Lab Manual, which was based off of Prof. Spencer Axani's Masters Thesis, accessible directly at <https://arxiv.org/abs/1908.00146>. However, this is a new detector, specifically designed to increase the CosmicWatch's physics, education, and industrial reach, as well as providing the backbone for a future citizen science project.

The original CosmicWatch project was significantly developed with co-collaborator Dr. Katarzyna Frankiewicz and Prof. Janet Conrad. The original project has had funding from the MIT Physics Department, the Wisconsin Particle Astrophysics Center (WiPAC), the National Science Foundation (NSF), and is now funded through the University of Delaware (UD).

We are excited to have the CosmicWatch detector incorporated into the Experimental Methods in Physics courses at UD. Developing this detector has been a passion, not just a hobby. We hope you enjoy it, and even consider building your own.

Many documents have played a crucial role in compiling this information. A great and valuable reference, is the Particle Data Group's (PDG) summary on cosmic rays [1] and energy loss in matter [2]. MIT Prof. Bruno Rossi's textbook, *Cosmic Rays* from 1964 [3], is a great entry-level resource, providing an early account of cosmic-ray physics investigations. It not only offers insightful reading but also allows readers to replicate many of the experiments conducted for the first time using the CosmicWatch detectors.

For a more contemporary perspective with a focus on history, Prof. M. Friedlander's book titled *A Thin Cosmic Rain* [4] is recommended. Dr. P. Grieder's comprehensive textbook, *Cosmic Rays at Earth* [5], provides an in-depth overview of cosmic-ray physics and will be frequently referenced. For higher-energy cosmic-ray physics, Prof. T. Gaisser's book (from the University of Delaware), *Cosmic Rays and Particle Physics* [6], proves to be extremely useful.

Chapter 2

SOURCES OF IONIZING RADIATION

Our discussion commences with an exploration of the diverse sources of ionizing radiation that can activate the Desktop Muon Detectors. Some forms of ionizing radiation hold particular significance due to their prevalence and energy levels. Additionally, we will touch upon why certain other forms of ionizing radiation do not register on our sensitivity, though a brief description of them is included for comprehensive understanding.

2.1 Cosmic radiation

The Earth is continuous bombarded by particles known as *cosmic rays*. About 74% (by mass) of this cosmic-ray flux originates from ionized hydrogen (free protons), 18% from helium nuclei (two protons and two neutrons), and the remaining portion consists of trace amounts of heavier elements [1]. A significant fraction of the observed cosmic-ray flux at Earth is relativistic, meaning that the individual nuclei possess kinetic energies greater than their rest mass ($E_k/mc^2 > 1$).

Lower energy cosmic-rays (GeV-scale) are significantly influenced by the solar wind and the Earth's geomagnetic field, as depicted in Fig. 2.1. These factors limit the flux interacting with the Earth. The high-energy flux extends up to 10^{11} GeV, beyond which cosmic rays lose energy through interactions with the cosmic microwave background, known as the GZK cutoff¹.

The energy of cosmic rays decreases rapidly: below 10^6 GeV, the flux decreases as $E^{-2.7}$, and above this, it steepens to approximately $E^{-3.1}$ [6]. To provide perspective, the number of 1 GeV cosmic-ray protons is 8.1 orders of magnitude higher than that at 1000 GeV (i.e., 2.7×3), or

¹The highest energy cosmic-ray observed, approximately 3×10^{20} eV [10] (48 joules), equivalent to a brick falling on your toe [11], was contained in a single proton and later named the *Oh-My-God Particle*.

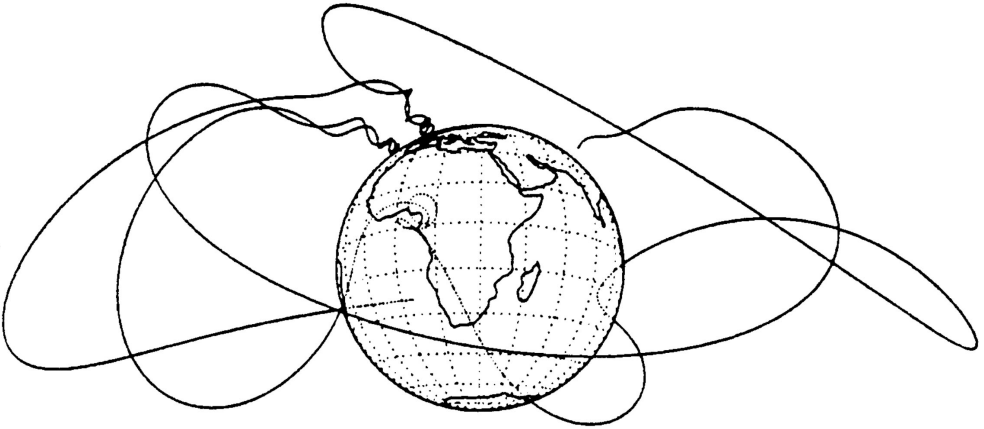


Figure 2.1: Simulated trajectories of low energy cosmic-rays interacting with the geomagnetic field. From Ref. [4]

16.2 orders of magnitude higher² than that at 10^6 GeV (i.e., 2.7×6).

When a primary cosmic-ray collides with a nucleus in the upper atmosphere (typically an oxygen or nitrogen nucleus), the energies involved can break apart either the primary particle or the target nucleus through nuclear interactions. The collision energy produces short-lived particles called *mesons*³. The most common mesons are the π -meson or pion (π^+, π^-, π^0) and the K-meson or kaon (K^+, K^-, K^0). Charged pions (π^\pm) decay within approximately ten billionths of a second, producing muons and neutrinos (charged kaons, K^\pm , are more complex in their decay, but they also preferentially decay this way or to pions). Neutral mesons (π^0, K^0) decay about one billion times faster (10^{-17} s) than charged mesons, primarily to gamma rays. Unlike neutral mesons, charged mesons can travel sufficiently before decaying to interact with another molecule in the atmosphere. This interaction may result in another nuclear interaction, similar to the primary cosmic-ray interaction, generating more mesons and contributing to the particle shower induced by the primary interaction.

Primary cosmic rays do not directly penetrate Earth's surface due to atmospheric shielding. However, a small flux of nuclear fragments (such as protons and neutrons) from these interactions can occasionally cascade down and reach the surface. Figure 2.2 illustrates a cosmic-ray interaction, with the initial interaction of vertical cosmic rays occurring at an altitude approximately between 15 and 20 km. Cosmic rays entering at an angle will interact at higher altitudes due to their path traversing more atmosphere [14].

The high energy photon from the decay of the neutral mesons quickly materialize into an

²The steep decrease in energy of the cosmic-ray flux necessitates large detectors for measuring rare high-energy events.

³Mesons, unlike protons and neutrons, contain only two quarks: one quark and one anti-quark. The lightest meson is the pion, followed by the kaon. Although there are many other quark/anti-quark pair combinations, their higher masses make them less preferentially produced and are not discussed here [12, 13].

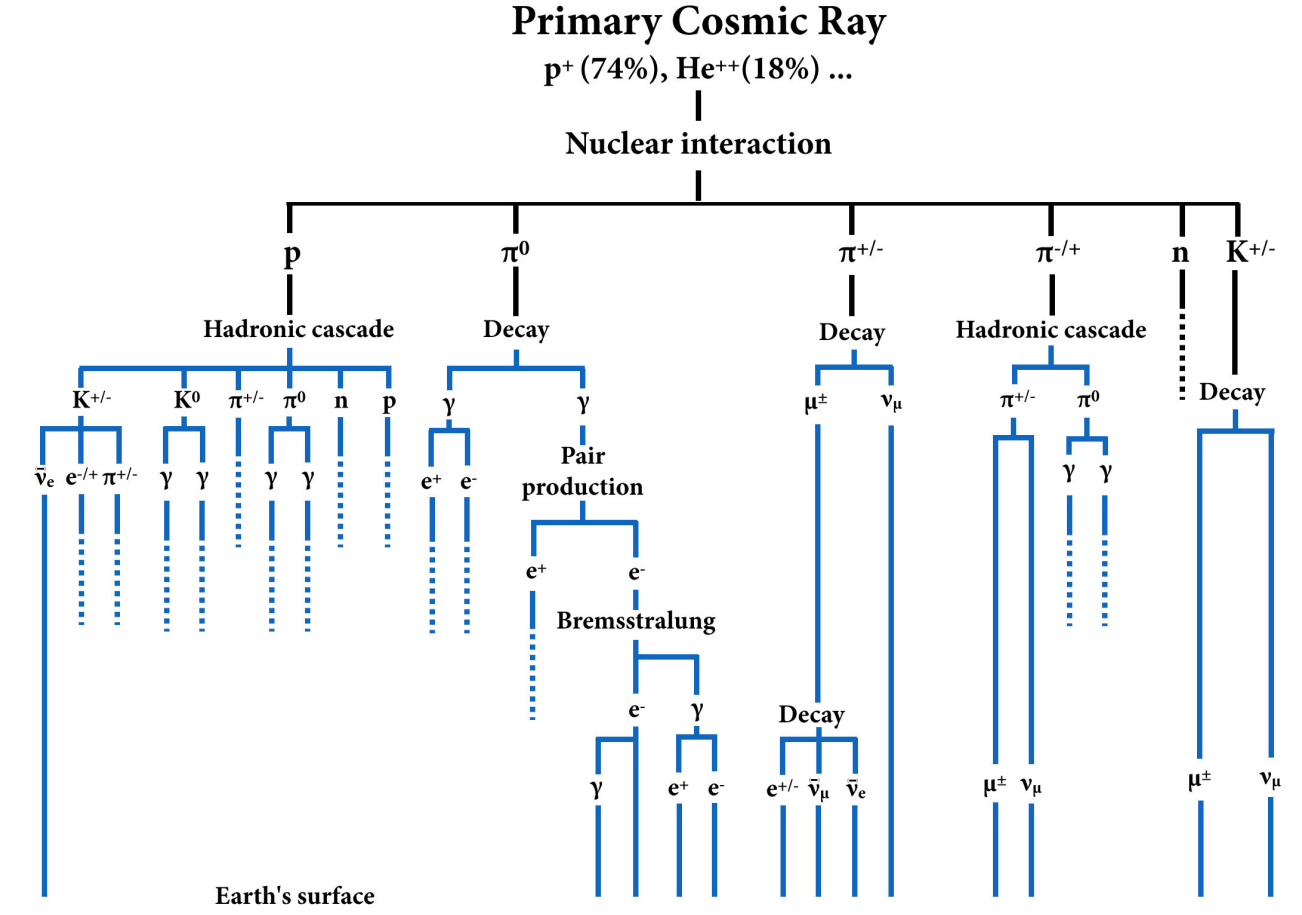


Figure 2.2: An schematic representation of the various decay and interactions chains that result from the interaction of a cosmic-ray in Earth’s atmosphere. This is a modified figure from Ref. [3].

electron-positron pair, also referred to as *pair production*. These electron-positron pairs then radiate high energy photons, which can again materialize into another electron-positron pair. This electromagnetic cascade process continues, dividing the original energy of the photons between the numerous electrons, positrons, and lower energy photons at the end of the cascade. Photons with energies less than 1.022 MeV cannot further pair produce and their interactions will be dominated by Compton scattering and photoelectric absorption. At lower altitudes, there isn’t a fresh supply of high energy neutral mesons due to the rapid decrease of nuclear interactions at lower altitudes.

The cosmic-ray muons (μ^\pm) originate from the decay of the charged mesons. A charged pion will decay to a same-sign muon (and muon-neutrino) with a branching fraction of 99.98%, whereas a charged kaon decays to a muon (and muon-neutrino) 63.5% of the time [15]. The neutrinos are not electrically charged and only interact through the weak force, therefore they can be fully ignored in this discussion.

$$\begin{aligned}\pi^\pm &\rightarrow \mu^\pm + \nu_\mu(\bar{\nu}_\mu) \dots (99.98\%) \\ K^\pm &\rightarrow \mu^\pm + \nu_\mu(\bar{\nu}_\mu) \dots (63.5\%) \end{aligned} \tag{2.1}$$

Approximately 80-90% of the muon flux in the energy range of interest (GeV to TeV-scale) comes from the decay of pions, and the remainder from kaons [16]. The muons are particularly penetrating, that is, they essentially only lose energy due to ionization as they travel through the atmosphere and other matter and can make it through a large amount of material. This is contrasted with *baryons* (particle comprised of quarks), which also interact through the strong force. This makes muons the most numerous charged particle showering down on the Earth's surface. Muons have a mass of 105.65 MeV and are also unstable particles with a half-life of 2.2×10^{-6} s. They decay to an electron and two neutrinos:

$$\mu^\pm \rightarrow e^\pm + \nu_e(\bar{\nu}_e) + \bar{\nu}_\mu(\nu_\mu) \dots (100.0\%), \tag{2.2}$$

however, again we can ignore the neutrinos. A cosmic-ray muon with an energy greater than 2.4 GeV will be sufficiently relativistic that its half-life, as seen by an observer on the Earth, will be dilated enough that it has a significant chance of reaching the Earth's surface before decaying. In other words, the muon decay length becomes greater than 15 km – the approximate altitude of the cosmic-ray muon production. Further, a typical muon will lose approximately 2 GeV of energy due to ionization as it passes through the atmosphere on its way to the ground. Combining these two facts with the fact that the geomagnetic field and interstellar solar winds drive back the GeV-scale cosmic-rays, as well as the steeply falling cosmic-ray energy spectrum, we can expect the average muon energy at Earth's surface to be greater than a few GeV. We typically quote the mean cosmic-ray muon energy at Earth's surface to be approximately 4 GeV [1]. The muons that do not survive the journey to the Earth's surface decay. The resulting electrons (or positrons in the case of a μ^+), also referred to as *Michelle electrons*, contribute to the low energy electromagnetic component from cosmic-ray showers at sea level.

Let us now compare the number of particles showering down on us at sea level. We'll limit ourselves to thinking about particles that are coming from one steradian about the zenith, this can be thought of as circular disk around the vertical (zenith) part of the sky whose area represents approximately $1/6^{th}$ of the total visible sky, or equivalently, a half-angle of 32° from the zenith. From this direction, we can describe the number of particles passing through a $1 \times 1 \text{ cm}^2$ horizontal surface per minute ($\text{cm}^{-2} \text{ min}^{-1} \text{ sr}^{-1}$) by following the measurements outlined in Ref. [1]. We expect approximately $0.4 \text{ cm}^{-2} \text{ min}^{-1} \text{ sr}^{-1}$ from μ^\pm with energies greater than 1 GeV; $0.2 \text{ e}^\pm \text{ cm}^{-2} \text{ min}^{-1} \text{ sr}^{-1}$ above 10 MeV, but the flux falls off fast with energy, becoming negligible above 1 GeV; and $0.0054 \text{ cm}^{-2} \text{ min}^{-1} \text{ sr}^{-1}$ from protons above 1 GeV; and a charged meson flux above 1 GeV two orders of magnitude lower than that of the proton flux. This means that the protons and charged mesons are insignificant at sea level, however, there is a significant muonic and low-energy electromagnetic component. In Ref. [5], the flux is divided into a hard component (essentially fully muons), which can penetrate 15 cm of lead, and soft component (approximately 60-65% muons and the remainder is electrons, positrons, and photons), which cannot. As we'll soon see, there are a variety of physical phenomena that influence fluxes, but the relative contributions listed here represent a useful approximation.

As we increase in altitude, the relative contribution from the ionizing radiation fluxes change. In particular, we see a larger contribution from both the protons and electromagnetic component, whereas the charged mesons are still sub-dominant. Once we pass the primary interaction region where the primary cosmic-rays are most likely to interact (typically around 15-20 km), the secondary particles produced by the initial nuclear interaction die off and we see a decrease in the ionization radiation flux. The shape of the curve describing the ionizing radiation flux as a function of altitude is called the Pforzner curve, and where the ionizing particle production reaches a maximum is termed the Regener-Pforzner maximum [17].

2.1.1 Flux variations due to solar system properties

There are several properties associated with the interstellar medium that modulate the cosmic-ray flux, and in particular the observable cosmic-ray muon flux. These properties are primarily associated with behaviour of the Earth and Sun's magnetic field.

The latitude effect: Roughly speaking, the Earth has a magnetic field that behaves similarly to a magnetic dipole orientated from north to south. The magnetic field points parallel to the surface of the Earth near the equator, and perpendicular to the surface near the poles. Particles traveling towards the Earth will be less deflected ($F = q\vec{v} \times \vec{B}$) near the poles compared to the equator. Low energy charged particles passing through the magnetic field may even become trapped in what's known as the *Van Allen radiation belt*. This presents a low energy cutoff, where the magnetic field is able to deflect protons below approximately 10 GeV near the equator (corresponding to a rigidity of 10 GV) and near 1 GeV at higher latitudes [18, 19].

The East-West asymmetry: The cosmic-ray muon flux is larger looking towards the west compared to the east due to the Earth's magnetic field. This is an effect produced by primary cosmic-ray particles being predominately positively charged. The positively charged muons curve towards the east, meaning that the intensity from the west is stronger. This effect is more evident in the upper atmosphere [5], and obviously a larger effect at the geomagnetic equator than at the poles.

Magnetic anomalies: There are local geomagnetic field variations, which causes a change in the cosmic-ray intensity. The most prominent being the *South Atlantic Anomaly (SAA)* [20], which extends from the east coast Brazil to the west coast of southern Africa (-50.0 to 0.0 geographic latitude and from -90.0 to 40.0 longitude). This is the region where Earth's inner Van Allen radiation belt extends closest to the planet's surface and provides the smallest amount of protection from cosmic-rays. In fact, the increased level of ionizing radiation when passing through the SAA is responsible for radiation damage to electronics on-board Low-Earth Orbit

(LEO) satellites⁴.

Solar modulation: The observed cosmic-ray flux at the top of the Earth's atmosphere depends partially on solar activity, which manifests itself as an 11-year cycle⁵. Solar winds can drive back low energy cosmic-rays entering the solar sphere and the modulation effect decreases with an increase in energy. According to Ref. [14], the 1 GeV cosmic-ray proton flux is twice as small during maximum solar activity compared to minimum solar activity; similarly there is a 10% reduction in the 10 GeV cosmic-ray protons during the solar maximum.

Solar Flares: Solar-flares can eject protons with energies up to several GeV, the upper end of which is able to produce muons through nuclear interactions. These events are rare transients, and since the energy is low, it primarily has an effect on the low energy muon flux [26].

2.1.2 Flux variations due to atmospheric properties

Similar to the previous subsection, there exists terrestrial phenomena that also modulate the cosmic-ray muon flux.

The Cosine Squared Law: At greater angles from the vertical, cosmic-ray muons must travel through a much larger distance, and therefore amount of matter, to reach a ground-based observer. A cosmic-ray muon traveling vertically downwards may only travel through 15 km of atmosphere, whereas one traveling in the horizontal direction must pass through approximately 500 km of atmosphere. The larger path length means that the muon will lose more total energy due to ionization in the atmosphere and also have a higher probability of decaying before reaching the ground. As a function of zenith angle, the cosmic-ray muon intensity is expected to follow a cosine squared dependence [1].

The atmospheric attenuation: Recall that the nuclear interactions between the primary cosmic-ray and atmospheric nucleus happen in the upper atmosphere. Therefore, particles reaching sea level must have had sufficient energy to penetrate the remainder of the atmosphere. An increase in atmospheric density (perhaps due to atmospheric pressure changes) will cause secondary particles to lose more energy as they propagate to the Earth's surface. Due to this, the muon rate turns out to be anti-correlated with the pressure (i.e. if the atmospheric pressure increases, the cosmic-ray muon rate decreases). The density of the atmosphere changes with the season and therefore exhibits a time-dependence. From other measurements, this is expected to be a percent level effect [27].

⁴The International Space Station (ISS) passes intermittently through the SAA [21] and has dedicated instrumentation for measuring the increased radiation dose to astronauts [22]. Astronauts from NASA missions as early as Apollo 11 [23] have also reported seeing flashes of light while being in orbit [24]. These flashes of light are attributed to high-energy particles in the space radiation environment, however many details on the origin are still unknown [25]

⁵There is also a 22-year cycle since the solar magnetic dipole flips polarity at every solar maximum, which occurs every 22 years [5]

The positive temperature effect: To produce a muon, we require a charged meson to decay. However, recall that the charged mesons are typically relativistic and have lifetimes on the order of nanoseconds⁶. This gives the charged mesons sufficient time to potentially interact with another nucleus in the atmosphere rather than decay. As the temperature increases, the atmosphere expands and there are fewer particles to interact with, thus increasing the probability of decaying rather than interacting [28].

Rather than correlating this with the ground based pressure (as in the paragraph above), it is more commonly correlated with atmospheric temperature – taking into account the temperature profile of the atmosphere. This effect is larger at higher energies and therefore is typically measured in laboratories located deep underground where the low energy cosmic-rays have less of an influence [29–31].

The negative temperature effect: As the temperature of the atmosphere increases, the atmosphere expands, moving the muon production region further out. This means that the muon path length increases, which gives them a higher probability of decay prior to making it to the ground. During the winter when the atmosphere is colder, shallower and more dense, cosmic-ray interactions happen closer to the Earth’s surface. The charged mesons quickly begin to lose energy and have a less likely chance of decaying into muons.

2.2 Radioactive backgrounds

The previous section described the ionizing radiation that we expect from showers of particles raining down from the upper atmosphere, and the expected phenomena that can modulate this flux. This section will describe ionizing radiation that originates on the surface of Earth and can also influence our measurements; we’ll refer to these as the *radioactive backgrounds*. Radioactive backgrounds are sub-divided into primarily three main processes called alpha, beta, and gamma radiation. Radioactivity is a quantum mechanical effect, which is non-deterministic, that is, we cannot predict when a particle will decay, rather we can only assign a probability to it. The energy scale of these processes are relatively low (MeV-scale) compared to the energies associated with the cosmic-rays (GeV and above), but their natural abundance on the surface of the Earth is sufficient that these are typically the dominant source of triggers in the Desktop Muon Detector.

Alpha decay is the result of an unstable nucleus ejecting a helium nucleus (a bound state of two protons and two neutrons), $(Z, A) \rightarrow (Z - 2, A - 4) + \alpha$. This is a quantum mechanical effect, where a helium state (helium is a very tightly bound state) forms in the nucleus, then quantum tunnels through the nuclear potential barrier, exiting the nucleus. The emitted alpha particle

⁶For example, a 5-GeV π^\pm produced at 15 km will travel approximately 300 m before decaying. This distance is small compared to the interaction path length of approximately 13 km, which means that most charged pions will decay rather than interact. However, at approximately 115 GeV, the pion has an equal probability to interact or decay in the atmosphere.

is mono-energetic, and since the helium nucleus has a charge of $+2e$ and mass of approximately 4 GeV (therefore, it moves slow and has a large charge), it will lose energy rapidly in matter. A 5-MeV alpha particle will have a range of 3.5 cm in air before losing all of its energy, or equivalently, 23 micrometers in aluminum⁷ [32].

Beta radiation is described as the decay of a neutron to a proton⁸: $n \rightarrow p + e^- + \bar{\nu}_e$. The proton remains in the nucleus, while the electron and electron-neutrino are ejected. Since this is a 3-body decay, the electron is not mono-energetic. It is emitted with a continuous energy spectrum whose maximum energy is approximately at the total energy available for the decay (the Q-value). Beta decays typically have energies that can range from tens of keV to a few MeV.

Gamma radiation is simply a high-energy photon, emitted during the de-excitation of an atomic nucleus. When the nucleus is in an unstable state (for example, maybe the nucleus absorbed a neutron or was left in an excited state after a beta decay), it will de-excite into a lower energy configuration releasing a photon. This is analogous to the de-excitation of an atomic electron, emitting a characteristic mono-energetic photon. Since the energy levels in the nucleus are quantized, gamma ray are also mono-energetic (with a small spread due to nuclear motion). These energy scales are in the 100 keV to MeV-range.

⁷The high energy loss rate that alpha radiation makes it useful for cancer therapies. An alpha particle will deposit all of its kinetic energy into a very local space (order micrometers in human tissue), which is capable of destroying cancerous cells.

⁸More fundamentally, during neutron decays, a down-quark in the neutron converts to a up-quark, emitting a virtual W-Boson $u \rightarrow d + W \rightarrow d + e^- + \bar{\nu}_e$. On the macroscopic level, this appears as the transmutation of an atom converting to another atom with an extra proton and one fewer neutron: $A(Z, N) \rightarrow A'(Z + 1, N - 1) + e^- + \bar{\nu}_e$.

Chapter 3

PARTICLE INTERACTIONS WITH MATTER

To identify a particle, it is essential for it to engage in an interaction with the detector's material, facilitating the transfer of energy from the particle to the absorbing substance. This segment will delve into the primary interactions that effectively transmit energy from particles like muons, protons, pions/kaons, and other high-energy heavy charged particles. Subsequently, we will explore interactions related to high-energy electrons (including positrons) and conclude with those associated with radioactive backgrounds.

3.1 High energy heavy charged particles

The following explanation proves valuable when considering any charged particles with a mass significantly greater than that of the electron ($m \gg m_e$). This encompasses all charged particles except for the electron and positron. For instance, the muon, the next lightest charged particle, is 206 times more massive than the electron. In contrast to the linear trajectories of heavy charged particles, electrons do not follow straight paths within a target, necessitating special consideration. The description provided below offers an approximation of the fundamental processes contributing to energy loss in matter, acknowledging that the scope of this topic is too extensive to cover comprehensively in a single document. More information can be found in Ref. [2, 8, 33, 34].

The rate of energy loss, often denoted as stopping power ($-dE/dx$), quantifies the amount of energy lost per unit distance traveled. It is commonly measured in units of MeV cm²/g, known as *mass stopping power*. To obtain the energy lost per centimeter, one simply multiplies this value by the density (in g/cm³) of the material being traversed. To facilitate comparisons, we express the energy loss rate in terms of water ($\rho = 1.0 \text{ g/cm}^3$), which conveniently shares a similar density with plastic scintillator. As a particle moves through a substance, its energy loss can be categorized into three mass-dependent ranges:

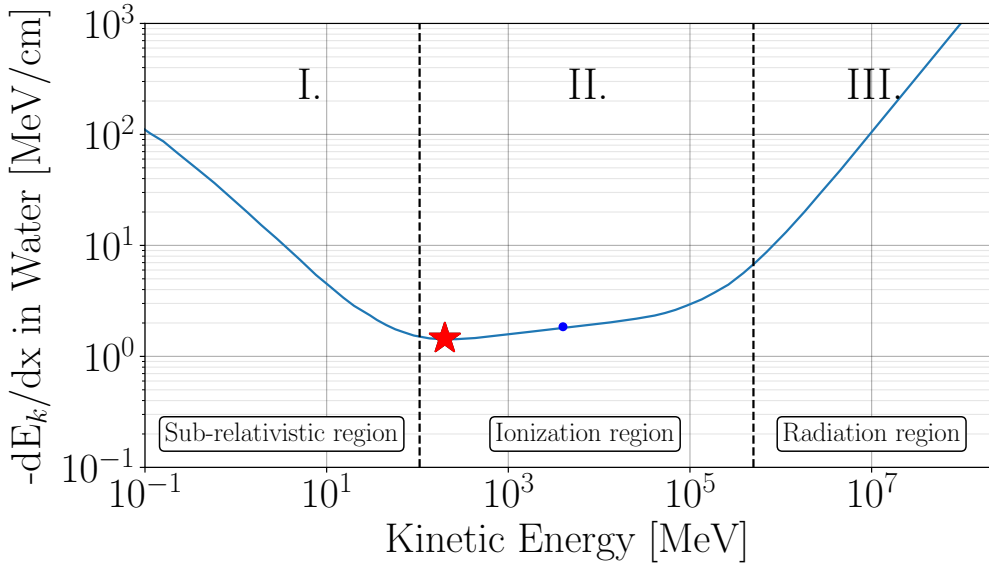


Figure 3.1: The kinetic energy loss per centimeter traveled, of a muon traveling through H_2O ($\rho = 1.0 \text{ g/cm}^3$). Modified from Ref. [35]. The blue dot represents the mean energy of the cosmic-ray muons at sea level (4 GeV), and the red star represents where the particle is minimally ionizing.

- I. The sub-relativistic region: ($E_k < mc^2$)
- II. The ionization region: ($E_k > mc^2$ and $E < 400 \text{ GeV m}^2/\text{m}_{\mu}^2$)
- III. The radiation region ($E > 400 \text{ GeV m}^2/\text{m}_{\mu}^2$).

The delineation of these three regions is depicted in Fig.3.1 for a muon traversing water. However, the energy loss can be adapted to another material by straightforwardly multiplying it by the density (in g/cm^3) of that material. For instance, the stopping power in lead would be adjusted by a factor of 11.34. Similarly, the energy loss can be tailored to a different particle by multiplying it by the square of the particle's charge. For instance, the energy loss of an alpha particle would be scaled by a factor of 4. While this plot is commonly presented in terms of momentum, we have scaled it using the kinetic energy of the incident particle for simplicity in explanation. The vertical dashed lines, marking the boundaries of the three regions, can be adapted to another charged particle using the aforementioned principles. For instance, a proton would enter the sub-relativistic region at approximately 1GeV.

In the **sub-relativistic region** (Muon: $E_k \approx 100 \text{ MeV}$; Proton: $E_k \approx 1 \text{ GeV}$), As the particle loses energy, the rate of energy loss per unit distance traveled increases. Essentially, this implies that once a particle enters this region, it rapidly decelerates and comes to a stop quickly. This phenomena is also known as the *Bragg peak* [7].

In the **high energy radiation region** (Muon: $E_k \approx 400 \text{ GeV}$; Proton: $E_k \approx 27 \text{ TeV}$), the

energy loss is associated with *bremsstrahlung*, pair production, and nuclear interactions, and scales linearly with energy. The radiation term becomes predominant at around 400 GeV for muons. However, it's important to note that the cosmic-ray flux decreases rapidly with energy. Muons in this energy regime constitute only a small percentage of the overall flux and experience rapid energy loss.

Finally, the **ionization region** encompasses the majority of the cosmic-ray muon flux. It is noteworthy that the mean muon energy at sea level is 4GeV, as indicated by a blue marker in Fig.3.1. The energy loss in this region results from ionization (breaking electromagnetic bonds) and excitation (raising the electron to a higher-lying shell within the absorber atom) of the incident particle. This behavior is described by the *Bethe Bloch formula*. Detailed explanations of the formula can be found in Refs. [7,8,35]).

This region is particularly fascinating because the energy loss rate remains nearly constant (increasing logarithmically), with an average energy loss rate of 2.2MeV/cm in a material with a density of 1.0g/cm³ across many orders of magnitude. The minimum point, denoted by a red star in Fig.3.1, designates the muon as a minimum ionizing particle (MIP), representing the energy at which the muon is most penetrating. The function exhibits such a flat trend in the vicinity of this minimum (up to approximately 400GeV) that any particle with energy near this red star is commonly referred to as a MIP. Interestingly, the majority of the cosmic-ray flux falls within this region. Consequently, to estimate the penetrating depth of a typical cosmic-ray muon, one can simply divide the energy by 2.2MeV/cm and multiply by the density of the absorber. For instance, a 10GeV muon can penetrate through approximately 17m of concrete (= 2.7g/cm³).

As for other heavy charged particles discussed in this document—protons, pions, and kaons—they also lose energy through ionization. However, due to their composition of quarks, they can also interact via the strong force. The strong force is responsible for nuclear collisions that can significantly impact the particle and its trajectory. This unique property makes muons stand out—they do not interact via the strong nuclear force, and being heavy allows them to penetrate through materials with minimal losses due to collisions with electrons in the absorbers and with minimal deflection in their trajectory¹.

3.2 High energy electrons/positrons and photons

As discussed in Section 2.1, a notable source of electrons/positrons with energies below 1 GeV showers onto the Earth's surface. This section focuses on describing the energy loss for high-

¹Given their ability to penetrate very large distances through materials, many experiments are situated kilometers underground to shield against high-energy muons. For example, the neutrino detector Super-Kamiokande is buried underneath a 1-km mountain in Japan to reduce the muon flux by a factor of 10^5 , preventing them from overwhelming the search for rare, less energetic interactions from neutrinos. Similarly, the IceCube neutrino detector is buried under 1.4 km of ice in the Antarctic glacier at the South Pole for similar reasons.

energy electrons, with the understanding that the explanation is equally applicable to positrons. For electrons above a few tens of MeV, radiation losses, primarily through *bremsstrahlung radiation* (translated as "braking radiation" in German), dominate the energy loss mechanism. Bremsstrahlung radiation involves the emission of photons when a particle accelerates and decelerates in the vicinity of the electric field of the material's nucleus.

A bremsstrahlung photon with sufficient energy can undergo pair production, yielding an electron and positron, which subsequently emit additional bremsstrahlung photons, initiating a cascade of electrons, positrons, and photons. This process governs the energy loss of the electron until its energy drops below a few tens of MeV, commonly referred to as the critical energy. Remarkably, the radiation energy loss rate scales with energy. In the region above the critical energy, the rate of energy loss (dE/dx) is proportional to the energy. Consequently, a 20GeV electron, for instance, initially loses energy per centimeter traveled at a rate 1000 times greater than a 20MeV electron, predominantly through bremsstrahlung radiation. This leads to a rapid decrease in the energy of high-energy particles as a function of distance traveled.

A *radiation length*, denoted as X_0 , is defined as the average thickness of a material that reduces the mean energy of an electron or positron by a factor of $1/e$ (Euler's number = 2.71828) due to bremsstrahlung radiation. In practical terms, this implies that an electron will lose a factor of e^{-t} energy after traversing t radiation lengths. For instance, after four radiation lengths, a 1 GeV electron will end up with approximately 20 MeV. The simplified *Heitler Model for electromagnetic cascades* approximates this by stating that one electron-positron pair will be created per radiation length, and each pair will receive half of the energy of the photon that produced them. After t radiation lengths, the cascade will contain 2^t particles (electrons, positrons, and photons), each with an average energy of approximately $E = \frac{E_0}{2^t}$ [36]. This concept is illustrated in Fig. 3.2.

A valuable list of radiation lengths for various materials is provided in Table 3.1. This table includes information about materials relevant to the Desktop Muon Detectors or used in some measurements below.

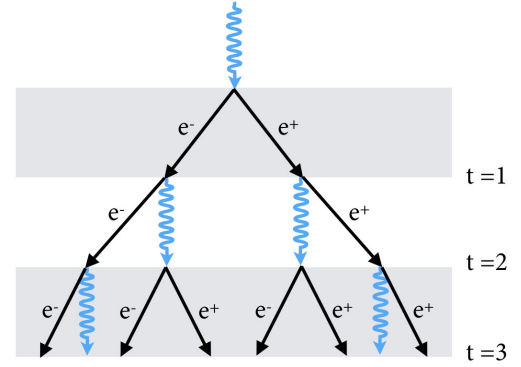


Figure 3.2: The Heitler Model for electromagnetic cascades.

3.3 Low energy electrons/positrons

Electrons and positrons, being the lightest charged particles, exhibit qualitative behavior in electron scattering distinct from that of high-energy particles in two ways. Firstly, the energy

Material	Density [g/cm ³]	Radiation length [cm]	Critical Energy [MeV]
Water (H ₂ O)	1.00	36.1	92
Lead (Pb)	11.35	0.56	9.51
Concrete	2.5	10.7	
Air at STP*	1.2931	30420	102
Scintillator (Polystyrene)	1.032	42.4	109
Aluminium (Al)	2.70	8.9	51.0

Table 3.1: A table of materials that are mentioned in this document and their corresponding radiation length. *STP indicates that the air is at the standard temperature and pressure: 20°C and 101.325 kPa. The data was collected from Ref. [1, 7].

loss by electrons fluctuates significantly more than that of heavy particles. For instance, the maximum transferable kinetic energy of a 4 GeV electron is the full 4 GeV (given their equal masses), whereas a muon with the same energy has a maximum transferable energy of approximately 1 GeV. Secondly, due to their small mass, electrons are particularly prone to experiencing large-angle deflections when scattering off a nucleus. This susceptibility is so pronounced that multiply scattered electrons may undergo a complete reversal in direction, a phenomenon defined as *backscattering*. The probability of backscattering is higher at lower energies, and if backscattered, electrons do not deposit all their energy in the absorbing medium. For instance, a 1 MeV electron has approximately a 10% chance of backscattering off a thick slab of aluminum, and a 50% chance of backscattering off a slab of gold. [37].

The previous section described electrons and positrons with energy above the critical energy of a material (typically tens of MeV), where their energy loss is completely dominated by bremsstrahlung radiation. At lower energies, electrons and positrons can inelastically interact through Coulomb collisions with atomic electrons to lose energy [38]. This leads to ionization and excitation, similar to the behavior observed in heavier particles. At even lower energies, in the MeV scale, electrons (positrons) also exhibit *Møller (Bhabha)* scattering.

3.4 Low energy gamma rays

Gamma-rays interact slightly differently from the charged particles due to their lack of electric charge. The three main interactions of gamma rays (and X-rays) are shown in Fig. 3.3.

An atomic electron can fully absorb the energy of a gamma ray², resulting in an electron with the energy of the initial gamma ray (MeV-scale) minus the binding energy of the atomic electron (eV-scale). This process is known as the *photoelectric effect*. As shown in Fig. 3.4, the photoelectric effect dominates for low-energy gamma-rays with a moderate-to-high density absorber.

²In order to conserve momentum, the photoelectric effect cannot occur on a free electron; it requires a nucleus to absorb part of the recoil.

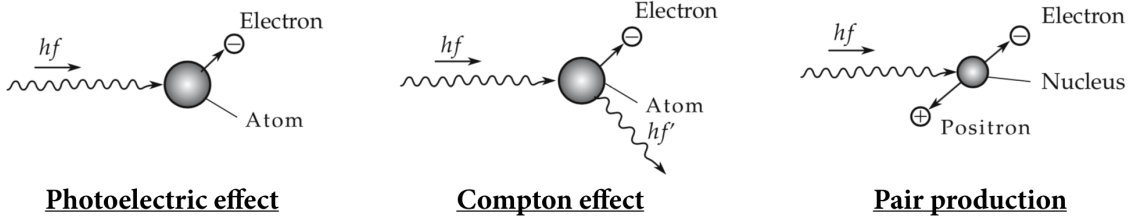


Figure 3.3: Modified from Ref. [32]

Compton scattering involves the partial transfer of energy from the incident gamma-ray to an atomic electron, leading to the electron's elevation to a higher energy level or ionization. The gamma-ray may alter its direction, exiting the material containing the electron, or it might undergo further scattering with another electron. Compton scattering prevails at low energy for materials with very low atomic numbers (Z), and the likelihood of scattering is directly proportional to the electron density, and thus, to the proton number of the material.

At energies above 1.022 MeV, electron-positron pair production plays a role. Pair production follows the same description as that found in the discussion of high-energy electrons (Sec. 3.2). The only difference is that the chain begins with a photon rather than an electron.

In addition, there are second-order effects, such as *Rayleigh scattering*, where the photon wavelength is large enough that it coherently scatters off the entire atom, and photonuclear interactions at higher energies that break up the nucleus [35].

3.5 Neutrons

Similar to photons, neutrons are not electrically charged, and thus, they do not undergo Coulomb interactions with electrons and nuclei. Instead, they interact through the strong force with nuclei. Due to the short-range nature of the strong force, these interactions are comparatively rare, as the neutron needs to approach the nucleus closely to interact. Several possible interactions are [7]:

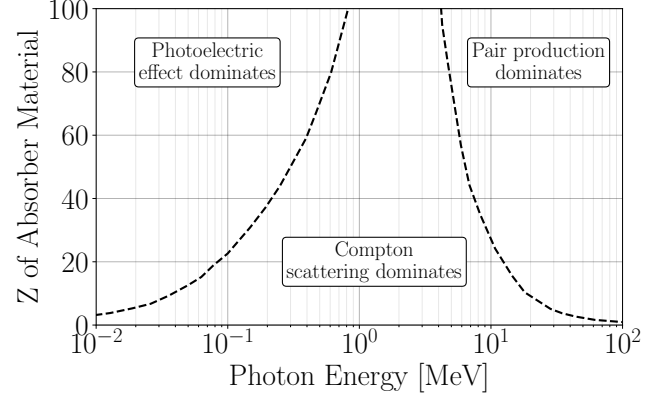


Figure 3.4: Dominant region for the three gamma ray interactions as a function of the photon energy and the target charge number Z . Modified from Ref. [8]

1. Elastic scattering off a nucleus
2. Inelastic scattering off a nucleus, leaving the nucleus in an excited state that may decay by emitting a gamma ray. To excite the nucleus, the neutron must transfer MeV-scale energies.
3. Neutron capture. At low energies, the neutron might be captured by the nucleus, emitting a gamma ray.
4. Fission
5. Hadronic shower, particularly at high energies (> 100 MeV).

High-energy neutrons produced in the primary cosmic-ray interaction will often collide with another nucleus, creating a similar interaction as the primary cosmic-ray.

Chapter 4

DETECTION METHODS

4.1 Single Photon Detection: Photomultipliers

Photomultipliers stand as one of the prevalent tools in the toolkit of particle physicists. These devices possess the capability to generate a measurable electrical signal triggered by the interaction of a single photon. The detection of photons allows us to extract information about incident particles by observing the photon emission as the particle loses energy within a material.

A widely utilized instrument for single photon sensing is the photomultiplier tube (PMT), known for its expansive photosensitive coverage at a reasonable cost. Despite its effectiveness, PMTs come with the downside of being bulky, fragile, and requiring high voltage. Other technologies, such as Avalanche Photodiodes (APD) and P-type and N-type semiconductor photodiodes (PIN photodiode), present their own set of advantages and limitations.

Recent advancements in silicon chip manufacturing have given rise to a new breed of photon detectors known as *silicon photomultipliers*, or SiPMs (also abbreviated as SPM). SiPMs bring several advantages over PMTs, including the ability to operate at low voltages (we'll use +30.0V), insensitivity to magnetic fields, robustness, and a compact form factor. Serving as single photon detectors, SiPMs exhibit peak responsivity near the emission peak of typical scintillating materials (420 nm). This modern technology is the foundation of the Desktop Muon Detectors.

SiPMs are composed of densely arranged *microcells* (see Fig. 4.1), where each microcell constitutes a distinct P-type and N-type semiconductor junction (P-N junction). During the formation of a P-N junction, free electrons from the N-type semiconductor diffuse towards the P-type semiconductor, and vice versa, leading to their annihilation. This process establishes an insulating region known as the *depletion region* at the boundary between the P and N-type semiconductors.

As a photon travels through the depletion region and imparts sufficient energy to a bound electron, the electron can transition to the conduction band, generating an electron-hole pair. Applying a potential difference across the P-N junction enables the energized electron to collide with other electrons, initiating their transport into the conduction band. If the potential difference exceeds a critical value ($> 5 \times 10^5$ V/cm), an electron avalanche or cascade (resembling a Geiger discharge) occurs, wherein a single electron gives rise to a current comprising millions of electrons. Once the flow of electrons begins, the silicon becomes conductive, and a quenching resistor reduces the potential difference across the P-N junction sufficiently to halt the electron cascade. Consequently, each microcell functions as a photon-triggered switch, allowing a brief flow of a small current if struck by a photon. The cumulative current flow is proportional to the number of triggered microcells and, hence, is proportionate to the incident photon flux (when the number of triggering photons far exceeds the number of microcells).

The Desktop Muon Detector utilizes a single On Semiconductor MicroFC 60035 C-Series SiPM, measuring 7.0 mm by 7.0 mm [39] (6 mm by 6 mm sensitive area). These SiPMs are most sensitive in the 420 nm range [40], corresponding to deep blue to purple light. I note that if the wavelength of a photon exceeds 1000 nm, the absorption length in silicon becomes too large, leading to the SiPM's size becoming impractical. On the other hand, if the photon wavelength is too short, it won't penetrate into the sensitive region of the SiPM, essential for effective detection.

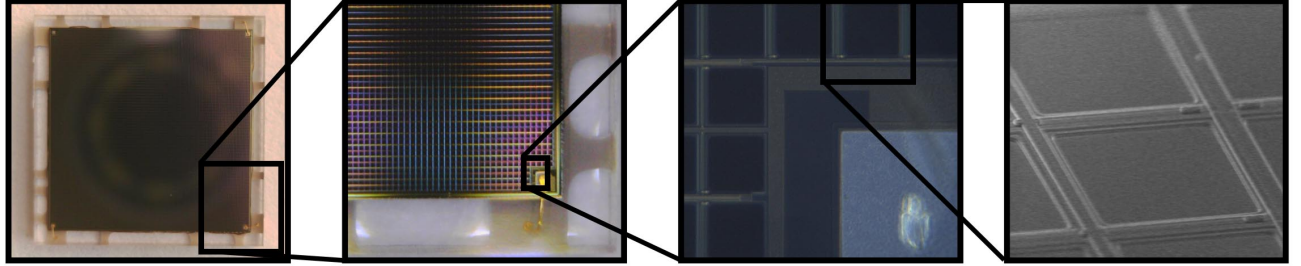


Figure 4.1: An image of an On Semiconductor SiPM [39]. Data sheets found in the datasheet folder. The SiPM has a length and width of 7.0 ± 0.05 mm and a thickness of 0.65 ± 0.05 mm. Each one of the tiled squares represents a single microcell, each of which operate independently in Geiger mode.

The applied potential difference is referred to as the "bias voltage," and it determines both the size of the region capable of producing the avalanche (the depletion region) and the energy gained by the electron-hole pair. The "breakdown voltage" signifies the voltage at which the voltage gradient in the depletion region is sufficiently large to initiate a Geiger discharge. For the C-series SiPMs, this typically falls between 24.2 and 24.7 V. If the bias voltage surpasses the breakdown voltage, the microcells will still operate in Geiger mode; however, the electron cascade in the P-N junction will carry more energy, resulting in a linear increase in the charge output (or gain). The disparity between the bias voltage and the breakdown voltage is termed *over-voltage*. It is recommended to maintain an over-voltage between 1.0 and 5.0 V. The Desktop Muon Detectors operate with an over-voltage of roughly 6.0 V, corresponding to a gain of approximately 6×10^6 [39]. At this bias voltage, the photon detection efficiency at 420 nm is

roughly 43%.

Thermal fluctuations have the capability to generate electron-hole pairs, mimicking single photon events. For our SiPMs, this phenomenon occurs at a rate of approximately 100 kHz per mm², or several MHz for the entire SiPM! This can pose challenges for applications relying on the distinction between small numbers of photons. It's noteworthy that the breakdown voltage needed to initiate the electron cascade is temperature-dependent; lower temperatures correspond to lower breakdown voltages (21.5 mV/C°). For every 8°C decrease in temperature, the dark rate decreases by a factor of two. Gain is also impacted by the temperature. For every degree C change, the gain decreases by approximately 0.8%.

4.2 Scintillators

Scintillators are materials designed to absorb energy through Coulomb interactions and subsequently re-emit that energy in the form of electromagnetic radiation, known as scintillation light. Scintillators can take various forms; for instance, they may be grown as crystals (referred to as inorganic scintillators) with added dopants, or they might consist of a fluorescing material embedded in plastic materials such as polystyrene or acrylic, or mixed into liquids like toluene or mineral oil—examples of organic scintillators.

Inorganic scintillators are typically more expensive, but they often have higher density and emit more photons per unit energy deposited. This characteristic makes them particularly useful for calorimetry. On the other hand, organic scintillators are generally more affordable since the fluorescent material is suspended in a common, often low-density material like plastic, facilitating ease of manufacturing.

Scintillators are highly valuable materials as they emit light in proportion to the energy deposited in the material. Consequently, a common metric used to assess the quality of a scintillator is expressed as the number of photons emitted per absorbed MeV of energy, often referred to as the scintillator efficiency. For instance, a typical organic scintillator may exhibit an efficiency (light-yield) of 10,000 photons/MeV. Another crucial parameter associated with scintillators is the photon emission profile, determining the wavelengths of emitted photons after de-excitation. Moreover, scintillators must be transparent to scintillation light to enable its propagation to the photon detector. Plastic scintillators may have attenuation lengths ranging from 0.3 meters to 3 meters [41, 42], while liquid scintillators like Linear Alkyl Benzene (LAB) can have attenuation lengths of up to 25 meters [43]. Scintillators also exhibit a very fast response and recovery, with excitation and de-excitation of the fluorescing molecules occurring on the order of nanoseconds for organic scintillators and hundreds of nanoseconds for inorganic scintillators.

The CosmicWatch Desktop Muon Detector was designed using an organic plastic scintillator, comprising a polystyrene base (essentially an inexpensive transparent plastic) mixed with a primary dopant of 1% by weight of POP (2,5-diphenyloxazole) and 0.03% secondary dopant

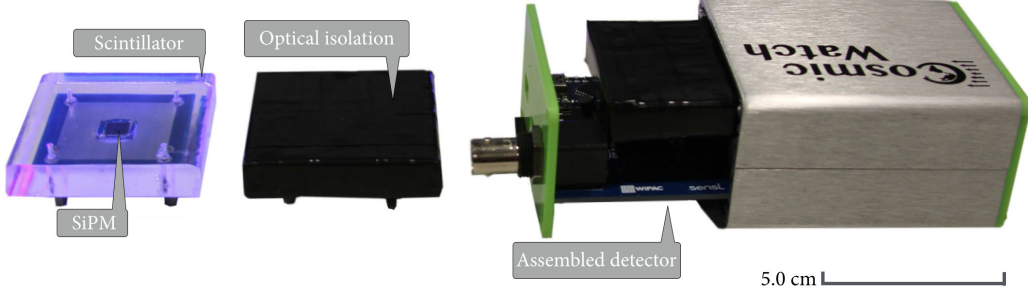


Figure 4.3: The components of the Desktop Muon Detector. Modified from Ref. [48].

POPOP (1,4-bis[2-(5-phenyloxazolyl)]benzene) [44]¹. This plastic scintillator does not emit light below 400 nm and has a maximum emission around 420 nm (deep-purple light). Developed by FermiLab for the MiNOS [46]/MINER ν A [47] experiments, we will focus on a description of organic scintillators below. However, a comprehensive description of inorganic scintillators can be found in Ref. [45].

The plastic scintillator consists of three essential components:

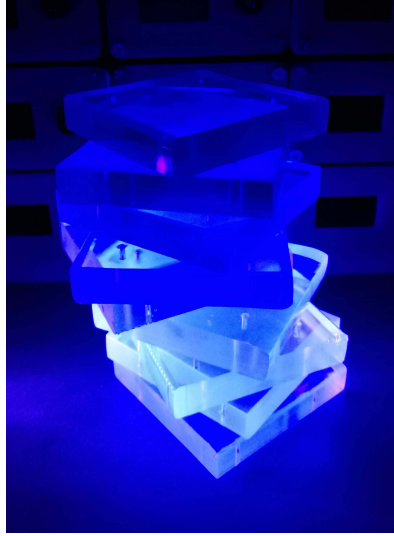


Figure 4.2: A UV flash light illuminating scintillator.

- A transparent base, visible in the visible spectrum, used to suspend the fluorescent material. This can be a type of plastic (such as polystyrene) or a transparent liquid like mineral oil.
- A primary fluorescing agent excited by the energy transfer from the incident charged particle. The de-excitation of the primary fluorescent material releases ultraviolet (UV) light. UV light has a limited travel distance in the base (on the order of millimeters) before being absorbed.
- A secondary fluorescent agent that absorbs the UV light and converts it to the visible spectrum. The visible light then travels through the scintillator, internally reflecting off the walls until it is absorbed. Ideally, some of the visible light will strike the photon sensor coupled to the scintillator.

A straightforward representation of the UV conversion process is depicted in Fig. 4.2. In this illustration, several pieces of scintillator are illuminated with a UV flashlight. The UV light is absorbed by the secondary fluorescent agent and re-emitted as deep blue/purple light. A polystyrene-based scintillator typically has a density of approximately 1.032 g/cm^3 (similar to water) and

¹Interestingly, PPO was one of the earliest compounds investigated as a scintillator solute by Hayes et al. (see Ref. [45]) from 1953-1958 and is still widely used

a refractive index at standard atmospheric pressure of $n = 1.581$ [8]. Recall, from your optics class, that air has a refractive index of $n = 1.00$.

The Desktop Muon Detector couples a SiPM (see Sec. 4.1) to a slab of scintillator through optical gel (and/or thin silicone pad), which reduces the probability of a photon being reflected at the interface by matching the refractive index from the scintillator to the housing of the SiPM, eliminating the air gap. Additionally, the remaining surface is wrapped in aluminum foil to reflect photons that escape the scintillator. The entire assembly is then covered with 2-3 layers of black electrical tape to ensure light-tightness. The assembly of the detector is illustrated in Fig. 4.3.

Chapter 5

THE COSMICWATCH DETECTOR

5.1 Introduction to the Detector

The CosmicWatch Desktop Muon Detector comprises a $5 \times 5 \times 1$ cm³ slab of plastic scintillator interfaced with a single photon sensor, known as a silicon photomultiplier (SiPM). When a charged particle traverses the scintillator and deposits some amount of its energy, a portion of that energy is re-emitted isotropically along the particle track in the form of photons. Photons reaching the photosensitive area of the SiPM can induce a Geiger discharge in the SiPM microcells. The microcells, when discharged, generate a small but measurable current. A single photon can trigger a single microcell (ignoring second-order effects), while multiple photons may trigger multiple cells. Through a measurement of the amount of current (or voltage, in our case) of the signal, we can infer the amount of energy deposited.

The SiPM signal (a pulse of current) is directed through a custom-designed printed circuit board (PCB), which amplifies and shapes the signal to make it suitable for measurement by an inexpensive micro-controller (MCU), a Raspberry Pi (RP) Pico. For each event, the RP Pico logs the event number, event time in seconds relative to the detector start time, whether or not the event was coincident with another detector (binary 1 or 0 respectively), the measured 12-bit ADC value of peak detector waveform, calculated SiPM peak voltage in millivolts (proportional to energy deposited), cumulative detector dead-time in seconds, temperature in Celsius, pressure in Pascals, and the x-y-z linear acceleration.

An array of complete CosmicWatch v3X detectors is shown in Fig. 5.1. The front of the detector is equipped with a reset button, two LEDs, and a built-in 0.96" OLED screen displaying information such as the total run time, number of events, and count rates (accounting for detector dead-time). The top 5 mm LED flashes on all events, while the bottom 3 mm LED triggers only on coincident events (events that simultaneously triggered connected detectors).

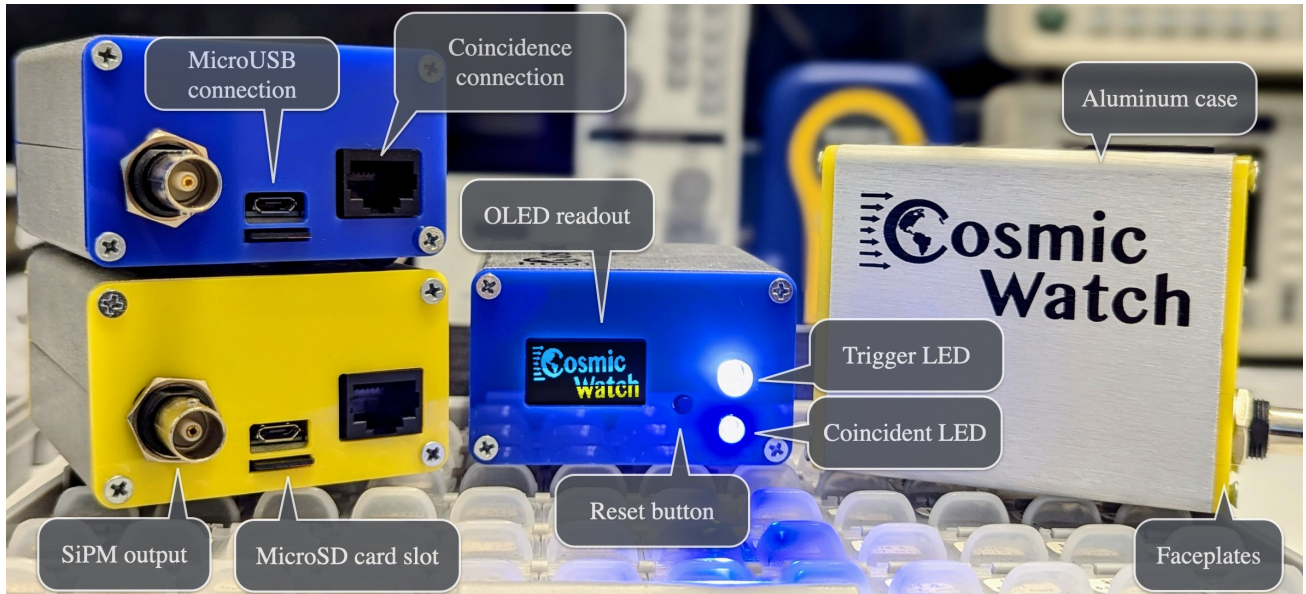


Figure 5.1: An array of the Desktop Muon Detectors.

The backside of the detector features a micro USB port on the RP Pico for powering the detector, uploading new firmware, or transmitting data to a serial port on a computer. It also includes an Ethernet connection for linking multiple detectors to perform coincidence measurements (see Sec. 5.2). The Ethernet connection will later be capable of communicating with a *CosmicWatch Expansion Module*, which will enable further use of additional peripherals, such as GPS, magnetic field sensors, realtime clocks, or anything that communicates over i2C, SPI, or UART. A microSD card socket under the USB enables a simply way to log the event-by-event data, with a new file being produced after each reset or power cycle. Additionally, a BNC connection connects directly connected to the SiPM output, and thus can be used to either inject pulses into the circuit or view the high fidelity SiPM waveform on an oscilloscope.

A single detector was measured to consume 0.5 W and can be powered through any USB connection supplying 1.8 V to 5.5 V. This could be a USB port on a computer, USB power bank, power outlet USB, or even a cell phone. The total mass of the detector, excluding the optional aluminum enclosure and end-plates, the detector has a mass of 83 g, whose measurements are illustrated in Fig. 5.2. Including the aluminum case, the mass is 200 g, and the case outer dimensions are 66.4 mm×70.0 mm×39.9 mm.

5.2 Setting detectors in coincidence mode

Many measurements in this document rely on the detectors operating in *coincidence mode*. This mode allows users to extra a rather pure sample of the cosmic-ray muon by rejecting events that likely came from radioactive backgrounds. Coincidence mode requires two detectors connected



Figure 5.2: Rough dimensions of the detector.



Figure 5.3: Two detectors in coincidence mode, powered by a USB power bank. In coincidence mode, every time a detector triggers on an event, it sends a digital pulse to the other detector. If the other detector also triggers on a pulse during at the same time, the event is said to be coincident and is very likely to have been caused by a cosmic-ray muon. Coincident events flash the coincidence LED (blue LED on the front plate).

together using an Ethernet cable (we'll refer to it as the *coincidence cable*). Once connected, only one of the detectors requires power; the other will be powered through the cable.

To set the detectors into the coincident mode, simply reset both detectors within a second of each other while they are connected together. Alternatively, you can unplug the power cable (microUSB) and plug it back in. The detectors will acknowledge the presence of a coincidence detector by brightly illuminating both LEDs on the front panel for one second. An example of two detectors being set up in coincidence mode is shown in Fig. 5.3.

All triggered events are recorded. However, coincident events will be designated in the data with a "1" in the coincident column (third column of the data), while master events have a "0" in its place. In coincidence mode, the OLED screen will display both the master and coincidence

rate.

Below about 5 km, coincident events are overwhelmingly likely to be due to a cosmic-ray muon, as backgrounds and accidental coincidences are unlikely to trigger both detectors simultaneously. A summary of why the purity of the cosmic-ray muon signal increases in coincidence mode is provided below.

- Alpha particles will not penetrate a single detector (either the aluminum enclosure or even the black electrical tape) and therefore cannot trigger both detectors at the same time.
- Beta particles (electrons and positrons) can be significantly attenuated by the aluminum case, and have a significant chance of scattering, thus losing energy. It's unlikely that the beta particle will be able to deposit sufficient energy within the scintillator (making it past the black tape and aluminum foil) in one of the detector, exit, then depositing sufficient energy in the second detector. However, there exists a rather substantial sub GeV electron/positron flux that develops in cosmic ray showers that has sufficient energy to trigger two detectors. This can be substantially attenuated by going inside a building, a floor or two of concrete does a pretty good job at eliminating this flux.
- Gamma rays can penetrate the aluminum enclosure and plastic scintillator, however they have a significant chance of Compton scattering (the dominant interaction), which will change the direction. If a gamma ray does interact with both detectors, this means that it likely Compton scattered off the scintillator slabs, lost sufficient energy to trigger the detector, then Compton scattered or photoelectrically absorbed in the second detector, also depositing sufficient energy to trigger that detector. This process will be rare, and represents a small part of the coincidence signal (an estimate of this rate is found in Sec. 9.5).
- Accidental coincidences, defined as two uncorrelated random events happening to hit both detectors within some time window, is also a rather rare occurrence at the standard background rates. This will be elaborated on in Sec. 7. The accidental coincidence rate scales linearly with both master count rates. As a rough figure, assuming both detectors have a 3 Hz trigger rate, the accidental coincidence rate is $54 \mu\text{Hz}$.
- A typical minimum ionizing muon passing through the slab of scintillator will typically deposit more than 2-3 MeV of energy in the scintillator, without being deflected. This is a rather large amount of energy compared to the common energies of radiogenic backgrounds (sub MeV-scale). If the muon passes through both scintillators, it will likely trigger both detectors simultaneously and be relatively bright in both detectors. Therefore, not only can we select these events out using coincidence logic, these events also tend to be brighter on average (more energy deposited in the scintillator means the SiPM peak voltage is larger). A histogram of the SiPM peak voltage (proportional to how much energy was deposited), is shown in Fig. 5.3, by plotting all events from a microSD card versus the subset of events that were labeled as coincidence ("1" in the coincidence column) and non-coincidence ("0" in the coincidence column). This figure can be recreated by running the



Figure 5.4: A histogram of the SiPM Peak voltage, of the full dataset from a single detector. The bump in the coincidence events, shown at roughly 50mV, would correspond to the average minimum ionizing muons, or an energy deposition of 1.5-3Mev.

plot.py script in the Data/ directory. This script requires you to have matplotlib installed. You can change the filename to plot your own data.

5.3 Recording data options

Data can be collected from the Desktop Muon Detector in many ways:

1. **(Recommended) Through a microSD card:** Each time the detector is reset or powered on, a new file on the microSD card (exFAT formatted) is created with a filename that counts sequentially upwards from the previous file. An "M" or "C" indicates whether the detector was in *Master mode*, indicating that a coincidence detector was not used during startup, or *coincident mode*, indicating that a second detector connected during startup. Extracting data using the microSD card is least prone to error and likely the simplest. To give you an idea of card size, one month of data is approximately 1 GB of data.
2. **Through the import_data.py script on your computer:** When the detector is plugged into a computer USB port, data is transmitted asynchronously at a baud rate of 115200 bps. Running the python script import_data.py (after you've installed the pyserial library), will allow you to save the data directly to a file of your choice. When run, the user is prompted to supply the path and name of the file to where the data is to be stored. It will then begin recording the data in real-time to that output file on your computer. The benefit here is that the computer will take a real-time global timestamp from the computer. It's likely that your computer syncs with NTP (Network Time Protocol), which provides

an accuracy to within roughly 1–10 ms. The RP Pico alone, will go out of sync with global time, at the rate of roughly 1 minute per day.

3. **Through a Serial Monitor on your computer:** There are also serial monitors available, that will allow you to see the data in realtime. I would say the simplest serial monitor is the ArduinoIDE¹, accessible by clicking on the top right magnifying glass icon, after selecting the RP Pico in Tools->Ports. However, recent updates to the ArduinoIDE make it difficult to copy and paste the data. Instead, I now prefer to use VSCode, after installing the 'Serial Monitor' expansion. The Serial Monitor is very useful when troubleshooting your detector. During bootup, the detector will print to the serial port a set of diagnostics, and might suggest where the problem is.
4. **Via the 0.96" OLED screen:** The OLED reports the total time represents how long its been (according to the RP Pico system clock), along with the number of master and coincident events, and their count rates (accounting for deadtime, of course). Therefore, if you simply need to know the count rate, and do not care about the event-by-event data, the OLED readout might be enough for your measurement. The OLED readout is shown in Fig. 5.5. In either mode, the first line reports the microSD file name, if there is one inserted. If in Non-Coincidence Mode, the last line reports the detector name.

The data on the microSD card or through the import_data.py script is saved in a simple to use .TXT file, in an easy-to-read format. Comments are always indicated with the "#" marker for ease of parsing. Each row is a different event, and each column represents some different property of the measurement. The columns are tab-delimited, to also make parsing easier. When the detector boots up, it first prints a set of diagnostics, measuring the voltage going to the SiPM, baseline, trigger thresholds and checking with peripherals. I'll expand on these diagnostics in an appendix (see Sec. ??). An example of the data is shown in Fig. 5.6. Each event is approximately 48 to 100 Bytes in size (depending on if you took the data on the microSD card or with the import_data.py script, respectively).

The data shown in Fig. 5.6 is formatted into tab-delimited columns, each of which is labeled in the header and defined as follows:

- **Event:** The event number of the detector. Sequentially counts upwards on each trigger.
- **Timestamp [s]:** The total run time (not livetime), measured in seconds. This is only accurate to roughly tens of seconds per day given the uncertainty by the precision of the internal clock.

¹<https://www.arduino.cc/en/software>

#	Event	Time[s]	Coincident[bool]	ADC[0-4095]	SiPM[mV]	Deadtime[s]	Temp[C]	Pressure[Pa]	X[g]:Y[g]:Z[g]
1	0.371086	0	227	14.8	0.000065	23.8	102287	-0.015:0.038:1.165	
2	0.533616	0	218	13.9	0.000439	23.8	102287	-0.013:0.039:1.174	
3	2.031897	0	330	24.1	0.000727	23.8	102286	-0.012:0.038:1.168	
4	2.543580	0	668	54.7	0.001009	23.8	102286	-0.014:0.041:1.172	
5	3.159818	1	898	75.7	0.001282	23.8	102285	-0.008:0.036:1.172	
6	4.025556	0	228	14.9	0.001562	23.8	102287	-0.011:0.037:1.164	
7	4.520926	0	299	21.5	0.001842	23.8	102287	-0.008:0.040:1.173	
8	5.603997	0	244	16.5	0.002140	23.8	102286	-0.014:0.034:1.171	
9	5.627472	0	202	12.4	0.002460	23.8	102286	-0.014:0.034:1.171	
10	7.178322	0	257	17.7	0.002705	23.8	102284	-0.017:0.042:1.170	
11	7.371780	1	1052	89.1	0.002995	23.8	102286	-0.016:0.037:1.172	
12	7.520026	0	542	43.4	0.003286	23.8	102286	-0.008:0.037:1.176	
13	9.263287	0	518	41.1	0.003564	23.8	102284	-0.017:0.034:1.170	
14	9.503008	0	215	13.6	0.003842	23.8	102289	-0.014:0.038:1.176	

Figure 5.6: Example data from a file AxLab_C_002.txt microSD card. This was the second file ("002") recorded in coincidence mode ("C") on the the detector named "AxLab." The definitions of the columns are listed in the header. Event 3 and 11 were identified as coincident events. Looks like the temperature where the data was taken was 23.8°C with a room pressure of 102 kPa. The last column shows the orientation of the detector. Looks like the z-direction linear acceleration was roughly 1.1 g, indicating that the detector was positioned upright.

- **Coincident:** If the detector observes a coincidence signal in the RJ45 connection (Ethernet connection) within approximately 3 us, the event is considered coincident, and this value is set to "1"; otherwise, it's "0." If at sea level, events with a "1" in this column are overwhelmingly due to cosmic ray muon interactions.
- **ADC [0-4095]:** The ADC measurement for the event. The RP Pico has a 12-bit ADC, meaning the values reported are from 0-4095 (2^{12} values). This corresponds to a voltage between 0 and 2.5 V (VRef).
- **SiPM [mV]:** The calculated SiPM peak voltage based on the ADC measurement. This number is roughly proportional to the number of photons that triggered the SiPM, and thus roughly proportional to the energy deposited in the scintillator.
- **Deadtime [s]:** The cumulative deadtime since the detector start. This must be accounted for when making any rate measurement. To calculate the event rate, divide the total counts by (total run time minus total deadtime). The denominator is what is called livetime, and represents the amount of time the detector was actively searching for events.
- **Temp [°C]:** The measured temperature of the detector via the on-board BMP280 temperature sensor. Measured in degrees Celsius.
- **Pressure [Pa]:** The measured temperature of the detector via the on-board BMP280 pressure sensor. Measured in degrees Pascals.

- **X-Y-Z Acceleration [g]:** The measured x-y-z acceleration measured in units of g, the acceleration due to gravity.

If you record the data through the import_data.py script located in the Data directory, it will add three additional columns. You will also notice that the data taken prior to running the import_data.py script is not saved in the file. Example data from this script can be found in Fig. 5.7. The additional three columns of data are:

- **Name:** This is the name of the detector. You can modify this in the config file of the microSD card. We print the name, since you can actually record from multiple detectors simultaneously through the import_data.py script into a single file. This allows you to determine which detector saw which event.
- **Time:** The global time from the computer.
- **Date:** The global date from the computer.

#	CosmicWatch: The Desktop Muon Detector v3X Questions? saxani@udel.edu											
#	Event	Time[s]	Coincident[bool]	ADC[0-4095]	SiPM[mV]	Deadtime[s]	Temp[C]	Pressure[Pa]	X[g]:Y[g]:Z[g]	Name	Time	Date
108	70.314277	0	528	42.0	0.044414	29.8	102264	-0.011:0.043:1.156	AxLab	10:02:04.597713	24/04/2025	
109	70.395089	0	297	21.3	0.044886	29.8	102264	-0.008:0.046:1.160	AxLab	10:02:04.678360	24/04/2025	
110	70.720457	0	194	11.6	0.045312	29.8	102264	-0.009:0.041:1.157	AxLab	10:02:05.003774	24/04/2025	
111	71.034092	0	453	35.1	0.045736	29.8	102264	-0.012:0.036:1.161	AxLab	10:02:05.317368	24/04/2025	
112	71.978173	0	973	82.4	0.046148	29.8	102264	-0.015:0.042:1.159	AxLab	10:02:06.261462	24/04/2025	
113	73.462418	0	402	30.5	0.046579	29.8	102264	-0.008:0.044:1.161	AxLab	10:02:07.745657	24/04/2025	
114	74.245910	0	360	26.8	0.046997	29.8	102262	-0.002:0.043:1.160	AxLab	10:02:08.529156	24/04/2025	
115	76.710032	0	246	16.6	0.047417	29.8	102265	-0.009:0.042:1.155	AxLab	10:02:10.993267	24/04/2025	
116	77.735197	0	529	42.1	0.047832	29.8	102263	-0.013:0.039:1.161	AxLab	10:02:12.018377	24/04/2025	
117	77.774267	0	668	54.7	0.048252	29.8	102263	-0.012:0.035:1.152	AxLab	10:02:12.057414	24/04/2025	
118	77.776174	0	532	42.4	0.048669	29.8	102263	-0.012:0.035:1.152	AxLab	10:02:12.059219	24/04/2025	
119	79.114436	0	207	12.9	0.049017	29.8	102264	-0.013:0.046:1.151	AxLab	10:02:13.397626	24/04/2025	
120	80.850632	0	293	20.9	0.049468	29.8	102264	-0.010:0.041:1.159	AxLab	10:02:15.133915	24/04/2025	

Figure 5.7: Example data taken from the import_data.py script. The three additional columns are highlighted in blue. They represent the detector name, the timestamp and data taken from the computer that is running the script.

Chapter 6

HOW TO BUILD A COSMICWATCH DETECTOR V3X

6.1 Overview

This chapter will go through how to build your own detector from scratch.

The construction of the detector will be divided into four parts. (1) Purchasing the components. (2) Populate the printed circuit boards (PCB). (2) Interface the SiPM with the scintillator. (3) Uploading firmware to the Raspberry Pi Pico micro-controller, testing, and your first measurement.

6.1.1 (1) Purchasing the components

All the components are listed in the purchasing_list.pdf document, located in the PCB directory of the GitHub repository. It includes the number of each component to purchase, along with a cost estimate for single purchases and 10x purchases, and a link to where the item can be purchased. We'll do our best to update this document as parts change name, however, nearly all components can be found through other manufacturers, except likely the SiPM. So, first, use the list to purchase the components. Next we solder the components to the board.

6.1.2 Populating the PCBs

Here is a step-by-step description of how to populate the PCBs. The components are almost all surface mount technology (SMT), which means that they are small and sit on top of the

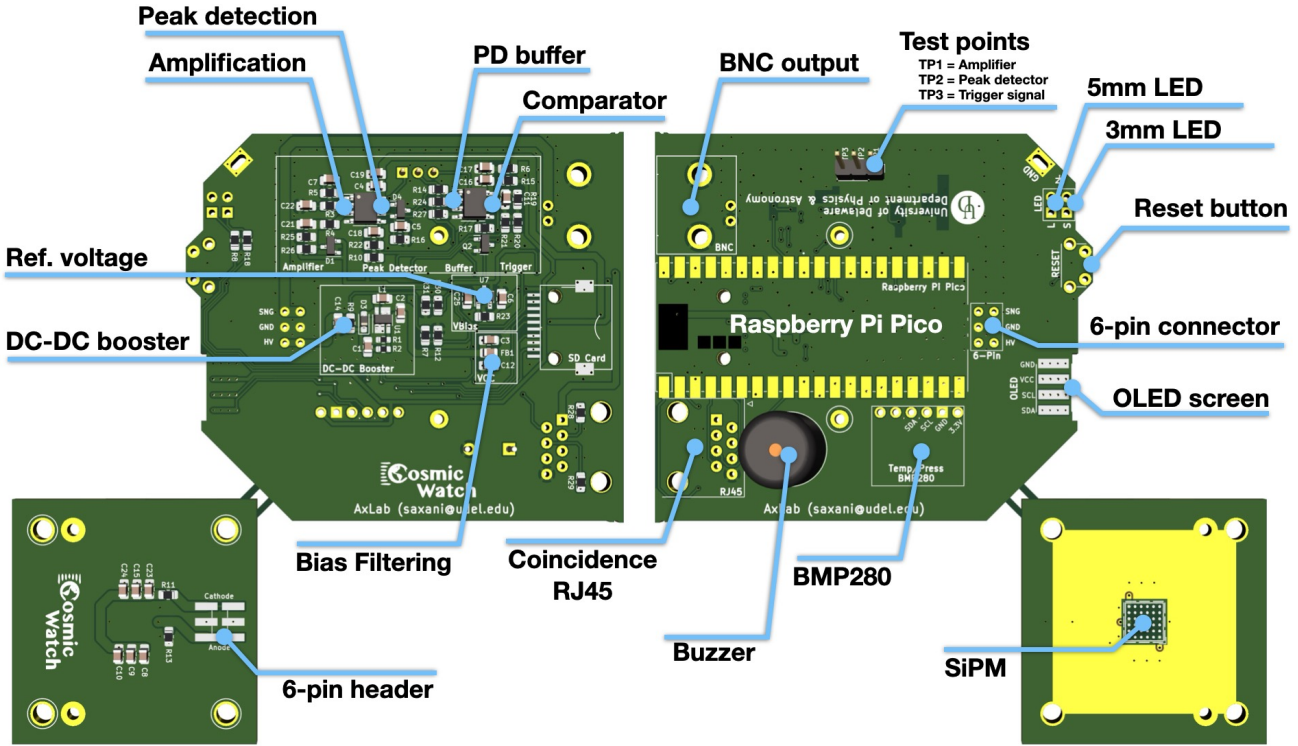


Figure 6.1: A 3D rendering of the printed circuit boards. Right: Top view. Left: Bottom.

board rather than with legs passing through it (through-hole components). With the exception of two resistors, we will be using 0805 SMT components. This represents the size, where the majority of the components are 0.08 inches by 0.05 inches. The first time you use them, they may look small, but you'll get used to them with a bit of practice. A pro may commonly use 0402 components or even 0201 components, more than eight times the size. The 0805 SMT components are a good size to learn about soldering.

All the components we'll need are listed both in the `purchasing_list.pdf` and the `Component_Placement_Sheet.pdf`, located in the GitHub PCB directory. The component placement sheet includes the identifier and the value of the component. This sheet shows you the preferred order in populating the main and SiPM PCB. It starts by teaching you how to solder using to master the easier components first, and it enables testing at each stage of the build.

We use the identifier R to represent resistors, C for capacitors, L for inductors, U for integrated circuits, and D for Diodes. Also note that the larger components, like the RP Pico, temperature/pressure sensor, and OLED, is drawn on the silk screen of the PCB in order to help you orientate the part. Make sure you put each component on the side of the board with its silk screen markings. A rendering of the PCB is shown in Fig. 6.1.

Soldering SMT components to the PCBs

Soldering involves melting a lead-based piece of metal (solder) to form the connection between the component and the PCB. While you can use your preferred soldering equipment, our preference is the **Hakko FX888DX-010BY soldering iron with the HAKKO T18-S4 soldering tip**, at a temperature of approximately 750°F. There exists non-lead based solders, but we've only found them to be terrible. We use **KESTER SOLDER 24-6040-0027 Wire Solder, 0.031" Diameter** solder. This soldering iron is hot, but not hot enough to damage the PCBs or components (except the plastic ones, like the housing of the BNC connector). You will hold the soldering iron with your dominant hand, and the solder with your sub-dominant hand. We call the components position on the PCB the "footprint," and each metal part of the footprint a "pad."

Tip: It's best to orientate the PCB rather than awkwardly orientate your hands while soldering. Move the PCB into a comfortable position for each solder joint.

Soldering a component in place always involves the same procedure for all components. Practice this routine with each component. The philosophy is to get one pad connected to the component, inspect the orientation, then when satisfied, continue with the other pad(s) and finally go back to the original one to clean it up. That is, the first solder joint is just to hold it in place for subsequent solders. It's easy to move a piece that only has one soldered joint, and very difficult if you have multiple pads constraining the component. Here's a more detailed procedure:

1. Determine the component you are mounting on the board from the component placement sheet. Find that component on the board.
2. Add solder to just one of the footprints pads.
3. Pick the component up with tweezers, bring it close to the footprint. Make sure that the component is flat against the PCB.
4. Melt the solder on the pad from Step 2. And bring your component into place with the tweezers. Keep holding it with the tweezers.
5. When in place, remove the heat, and let the solder solidify. Then, let go with the tweezers.
6. Inspect. Is it flat against the board? Is it in the correct orientation?
7. Finalize. If it looks good, solder the other connections. If it doesn't, melt the solder on the single pad and re-orientate.
8. Perfect. Now that the component is secured to the board, you can go back and add new solder to the joint to ensure a good connection.

Follow and master the above. By the end, you should be able to add a single component in seconds.

NOTE: some components have a direction. We've noted it on the reference list. Diodes have directions. The integrated circuits (IC) have direction.

If you are comfortable with build already, you may prefer to use the purchasing list to populate the board. If it's your first or second time, we would suggest using the Component_Placement_Sheet.pdf. We've made this list such a way that the first components are good to learn on. You should pretty easily get to Step 5 without many difficulties. If at any point one of the tests isn't working, it means that you either misplaced a component (unlikely) or you have a poor or missing solder connection on a component (very likely). The first step to troubleshooting will always be to check the solder joints. Add some fresh new solder to joints, to make sure you have good, solid connections. At this point, you need to mount the SiPM. Since the SiPM represents half the cost of the detector, we will describe the procedure in verbose below.

Mounting the SiPM

The hardest component to mount is the SiPM. First, you need to make sure you have the SiPM correctly orientated. There is a fiducial marking on the SiPM PCB (white L-shape, lower-left relative to the text on the PCB). This lines up with the Pin 1 of the MicroFC SiPM. Pin 1 is hard to identify, but it is represented by an extra metal leg sticking radially outwards on the side of the SiPM. Have a look at Page 10 of the MicroFC documentation if needed. Here's the procedure for mounting the MicroFC SiPM:

1. Add a small bump of solder to pad one of the SiPM footprint on the SiPM PCB.
2. Pick up the SiPM with your fingers. Avoid using tweezers, as they may scratch the surface.
3. Identify Pin 1 on the SiPM, orientate it with the PCB fiducial marking.
4. Use your fingers to hold the SiPM, perfectly aligned to the silkscreen drawn on the PCB, while you heat the bump of solder. Once it melts, the SiPM should be lying flat against the SiPM PCB, secured in place once the heat is removed.
5. Inspect orientation. If misaligned heat the pad with the bump of solder and adjust positioning. Else, add solder to the other pads. The solder will flow under the SiPM and connect the legs.

Testing the SiPM connection The SiPM acts as a diode. That is, it allows current to flow in only one direction, and has a voltage drop. Measuring the voltage drop between the Cathode and Anode (positive terminal on the Anode and negative terminal on the Cathode) on the SiPM PCB (annotated on the back of the PCB) tells you if the SiPM is connected. Using the diode setting on a multimeter, you should see a voltage drop of approximately 0.5 V. If you do not see the voltage drop, it could be (1) that you have the component orientated incorrectly (Pin 1 on the SiPM is not on Pad 1 of the footprint), (2) the solder is not fully connecting the SiPM to the board, (3) you have your test leads on the multimeter backwards, swap hands and try again. You want to make sure the SiPM is connected before continuing. If it is not, removing all the tape later takes quite a bit of time.

With the SiPM mounted, Step 6, you are essential done with soldering and you now need to put the pieces you built together. Attach the two standoffs to the SiPM PCB. We will now cut and interface the scintillator.

Cutting the plastic scintillator

You'll need to cut (or purchase) a $5\text{cm} \times 5\text{cm} \times 1\text{cm}$ piece of scintillator. I cut the scintillator on a Mill, so that you get a nice smooth surface from the end mill. I prefer to use a 3/4" two flute end mill at 1000 rpm, however just about anything will work. Then, after cutting to the correct size, I drill, using a number 48 bit (diameter = 1.93 mm) the four holes, in a square pattern with length 30 mm. Finally, I melt (heat treat) the milled opaque surfaces using a hot air gun. This will make a nice transparent surface that will help promote total internal reflection (the more photons you collect, the better your detector can estimate energy deposited). The dimension of the scintillator can be found in the CAD folder of the GitHub repository.

Interfacing the SiPM to the scintillator

Once you have all the components populated, including the SiPM, it's time to interface the SiPM to the scintillator. Make sure you have the aluminum standoffs on the SiPM PCB, securely fastened (past hand tight) with the size 0 screw.

First, wrap the scintillator in a single layer of aluminum foil, leaving a roughly $2\text{x}2\text{ cm}^2$ open area for the SiPM face. Add a small amount of black electrical tape to hold it in place, as shown in the Fig. ???. It's hard to see the four mounting holes with when the scintillator is wrapped in aluminum foil; you can simply apply some pressure to the location of the holes to have their outline pop through the foil/tape. I would use something sharp (liek the tip of the tweezers) to poke holes through the foil/tape, to help align the SiPM board.

Apply a generous amount of optical gel (silicon-based optical PMT coupling gel) to the surface for the SiPM. Drop in the four #2 screws in to the outermost SiPM PCB holes, and screw the

board into the scintillator. Remember that the SiPM is roughly 0.65 mm thick, so there should be a gap of roughly that size between the PCB and scintillator. Silicon optical gel can be tough to find, I've used simple silicone pads, which worked alright. Really, you want something with an index of refraction of 1.4 that will break the air barrier between the SiPM and scintillator.

Finally, with the SiPM screwed into the scintillator, you now need to wrap it in black electrical tape. Remember, we are looking for only a few photons, so we need this thing to be fully optically isolated. Even the smallest light leak will let millions of photons per second, prohibiting you from seeing the small flashes of light produced by particles running into the scintillator.

Tip: do a good job wrapping the scintillator. Cut the corners of the black electrical tape such that they fold over nicely. Best to wrap well once, then try to fix it later.

Uploading the firmware

This is pretty simple. You need to program the micro-controller so that it knows what it's doing. Follow these steps to upload the firmware to the RP Pico. If you want to know how the firmware works, we've described it in Sec. B:

1. Hold the boot select button down on the RP Pico while plugging it into a computer. This is a little white button on top of the board.
2. Release the button.
3. The RP Pico will appear as a removable drive on your computer. If it doesn't make sure you read Step 1 correctly. If it still doesn't work, it's likely because your USB cable does not have data-transfer. You might need to find a better cable. Some are just for power.
4. Open the drive.
5. Drag and drop the CosmicWatch_v3X_22.uf2 file from the Firmware directory in the GitHub, into the drive.

If the firmware was uploaded correctly, the RP Pico will disconnect from your computer, and you should see your OLED screen on your detector light up.

If the full construction went according to plan (probably 30% chance that you won't run into problems), you should be able to plug your SiPM and scintillator combo into your Main PCB. When you supply power to the RP Pico, the detector should trigger at roughly 2.5 Hz. The master rate will depend on how well you build the detector. Essentially, the detector triggers on some number of photons, and the number of photons that the SiPM sees will depend on things like the quality of the surface you heat treated on the scintillator, the optical coupling,

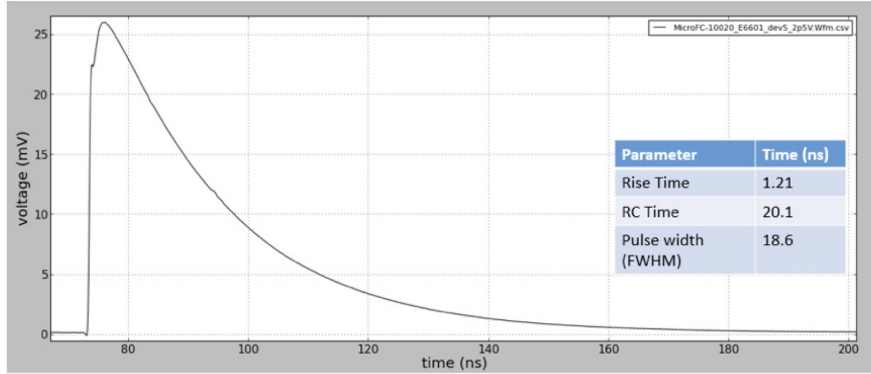


Figure 6.2: A typical SiPM pulse. Given the scale, I estimate this is about 100 photons given a gain of 4×10^6 .

the scintillator-to-scintillator light yield differences, that quality of your aluminum foil. About 0.4 Hz of this rate are muons; the rest is mainly backgrounds related to environment radioactive decays. If you like, you can insert the detector into the case, add the LED holders to the front face plate, and rubber feet to the bottom of the case. The case is purely cosmetic and protective. If your measurement does not need a case, you can run the detector without it.

The fun begins when you have two detectors built. When booted up together, and plugged in with an RJ45 cable, they will talk to each other. Both detectors will flash a bright LED pulse for 1 seconds, indicating that they see each other and have entered "coincidence mode." In coincidence mode, events that are observed by both detectors (within a three microsecond time window) are tagged as coincident and are overwhelmingly very likely caused by a cosmic ray muon passing through both detectors.

Note: when you supply power to one of the detectors, the RJ45 cable powers the second detector.

Troubleshooting

If you followed the component_placement_list.pdf, you would have hit various checks to test different parts of your circuit. For this section, we'll assume you ran into some problem that you couldn't resolve, and describe common troubleshooting techniques.

- **I see smoke from the MAX5026 DC-to-DC booster.** Disconnect immediately. The component is on backwards. You may have fried it. Maybe not though. You need to take it off and double check Pin 1 of the MAX5026 lines up with Pad 1 on the main PCB.
- **I'm not seeing +30V between the HV and GND 6-pin connector going to the SiPM.** This will be caused by a problem in the DC-DC booster area of the PCB. First,

check the orientation of the MAX5026 DC-DC booster. Make sure you have greater than 3 V across C2, this is the voltage coming from the RP Pico, used to power the circuit. R2 and R1 set the HV output voltage. Are they connected?

- **I have +30V going to the SiPM, but I don't see any 10mV, 100ns pulses out of the BNC connector (example pulse shown in Fig. 6.2).** First make sure that you are correctly setting up the oscilloscope; set the vertical scale to 10 mV per division and the horizontal scale to 200 ns per division. Set the trigger to 10 mV on the correct channel. I also set the trigger to Normal rather than Auto. You should see pulses triggering the oscilloscope at the hertz level. If you still don't see anything, your problem is with the SiPM PCB. You likely have one of two issues. The smallest light leak will cause problems. Small light leaks will look like a lot of noise on the oscilloscope. Add some additional tape, look for holes in the corners, et cetera. Otherwise, the problem could be with the SiPM, which isn't great, since you have to unwrap the scintillator to check it. The most common problem is that you mounted the SiPM in the incorrect orientation, or a poor connection on the SiPM. Before wrapping up the SiPM scintillator, it's good to check that you have approximately a 0.5 V voltage drop between the Anode and Cathode of the SiPM PCB. This is a good way to test if your SiPM is connected.
- **I see pulses out of the BNC, but my detector isn't triggering.** If this is the case, it means you have a problem with either the amplifier, peak detectors, or trigger circuit. We can use the test points (TP1, TP2, TP3) to identify the problematic area. First, setup the oscilloscope to trigger on the output of the BNC, then connect the scope probe to channel two. We will use channel two to look at the signals on TP1, TP2, and TP3. and see if you have 50x amplification on TP1 and 250x amplification on TP3. If no, that narrows down the problem to the respective amplifiers. If it looks good, check TP4, the high gain peak detector. You should see pulses that are 250x larger than the output of the BNC, but they decay over 100s of microseconds. If you see this, your detector should be triggering, if not, make sure you have the correct software. You can also check TP2, the low gain peak detector. This should be 50x larger than the BNC pulse, but also decay over 100s of microseconds.
- **I see a high power draw (>0.7W).** You have a short somewhere, a misplaced component, or component with the incorrect orientation. Disconnect immediately and go through your circuit again. The most common mistake is mounting the LT1807 op amp backwards. The pin 1 needs to be on the correct side of the footprint. You can often identify the problematic component by touching various parts of the board. None should be hot. If hot, there's likely a problem in that area.

6.2 Taking your first data

When conducting a coincidence measurement, careful consideration of what is being measured and how the orientation impacts the measurement is crucial. For instance, when interested in

the angular spectrum of cosmic-ray muons, the goal is to selectively accept muons originating from a small solid angle (a specific area of the sky). Fig. 6.3 illustrates several possible configurations. On the left side of Fig. 6.3, labeled as (a), two detectors spaced a few centimeters apart are connected with a coincidence cable. In this setup, only muons traveling downward through the blue area can trigger both detectors (consider the trajectories that can trigger both detectors). This configuration is suitable for measuring the angular distribution of cosmic-ray muons. Fig. 6.3 (d) depicts a configuration where both detectors will trigger from down-going muons over a much larger solid angle (nearly full sky). This configuration is commonly employed to extract strictly muon rate information, as it provides the highest statistics by examining the largest solid angle. The configuration essential turns the detectors into a muon telescope.

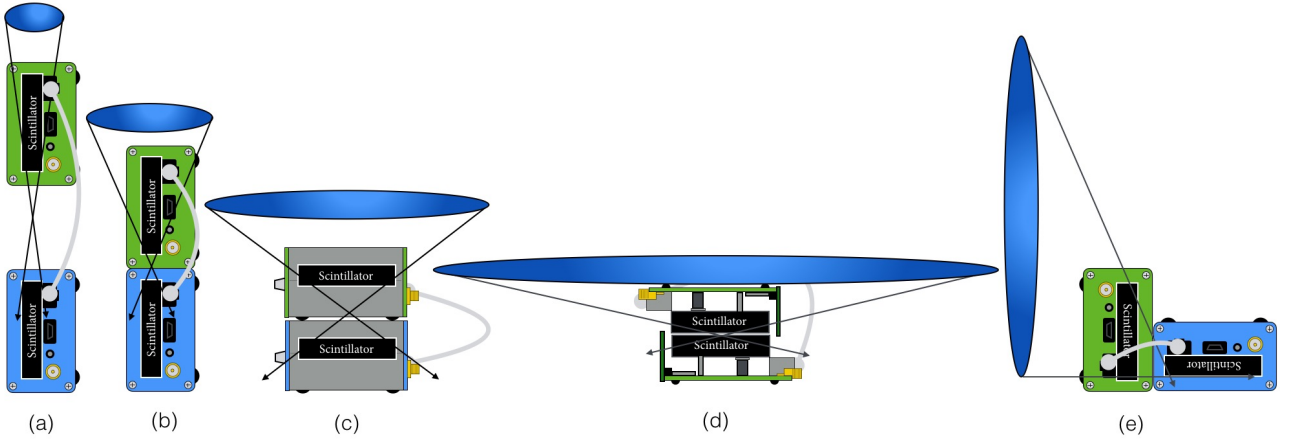


Figure 6.3: This figure shows several configurations for setting up the detectors in coincidence mode. Moving from left to right the solid angle subtended between detectors increases (illustrated as the blue ovals above the detectors) as well as the coincidence rate as measured by the coincident detector.

Let's take our first set of data in configuration (d) of Fig. 6.3, in near the center of a building with roughly a foot of concrete floors above, shielding out the electromagnetic component of the cosmic ray showers (see Sec. 6.3.1). We'll let the detectors sit untouched taking data over 24 hours. First, let's look at the OLED screen.

We see that both detectors have the same coincidence rate (bottom line on the screen). This is because they have the same number of n

6.3 Things you should understand

When conducting measurements with the Desktop Muon Detectors, it is essential to consider a few key factors.

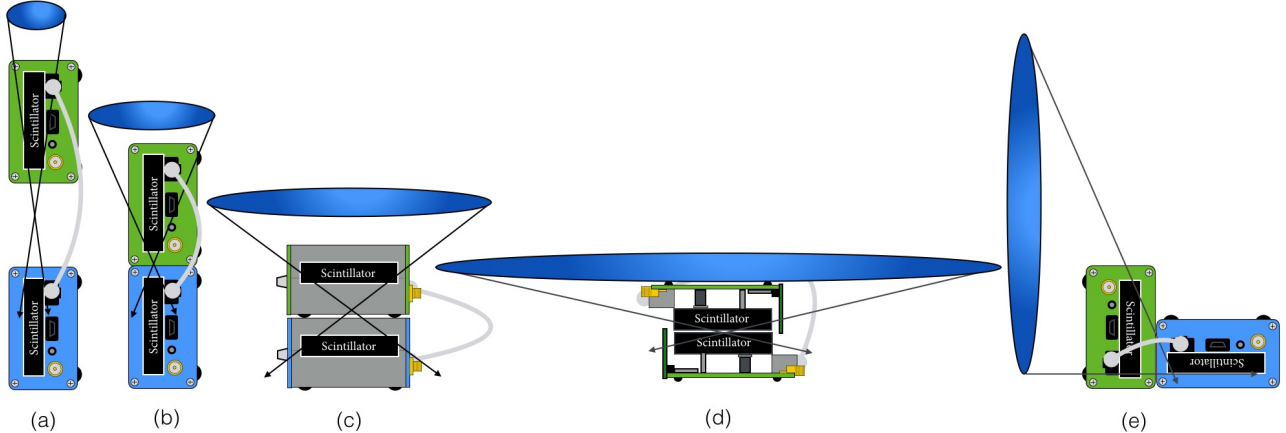


Figure 6.4: The OLED screen readout after 24 hours in configuration (d).

What is deadtime?

The RP Pico is an inexpensive (4 USD) and relatively slow device compared to other much more expensive devices. While being a fairly new MCUs, inherent issues arise due to its speed limitations. An important aspect of any rate measurement with any detector is that every command, whether it involves simple arithmetic or printing detector information to the serial port or microSD card, takes time to execute. If during that time, the detector cannot monitor for incoming signals (i.e. it is dead), you need to account for that time. The term associated with the time during which the detector is unable to make a measurement is referred to as *deadtime*. The detector software code calculates the deadtime by measuring how long each command (or sets of commands) takes. The cumulative deadtime up to the event you are looking at is recorded in the data output. To obtain an accurate measurement of the time the detector was able to make a measurement, the deadtime must be subtracted from the total runtime; the result is termed *livetime*. Deadtime is a common feature in nearly all particle physics detectors. It becomes more problematic as rates increase as well, as part of the deadtime might be associated with creating and reading out the event. At sea level, the deadtime may affect the rate by 0.5%, while in a high-altitude balloon at 60,000 feet, where the count rates approach 60 Hz, the deadtime impacts the rate measurement by roughly 3%. We strategically use dual cores with specially data buffering techniques to reduce the deadtime as much as possible. For context, the deadtime per event is more than two orders of magnitude lower than the previous published version of the detector.

6.3.1 Discussion about backgrounds in a set of coincidence events

Is the purity 100% muons?

Electromagnetic contribution from the shower

Looking at Fig. 2.2, you might wonder what other particles are able to trigger the detectors. Well, at sea level, I would argue that there is a population of low energy (sub-GeV) electrons that cascade down and are capable of triggering two detectors in coincidence. In fact, outside, in open air, with no overburden (overhead shielding), this is approximately 0.1 Hz, or around 30% of the coincidence rate. The good news is that you can simply move under some concrete to shield the detectors from this component of the flux. If you want to make a pure muon measurement, make sure to go under a foot of concrete or more to get rid of this low energy electromagnetic component of the flux.

Proton contribution from the shower

: At sea level, maybe 1 in a 100 recorded coincident events will actually be a proton. You can't really get rid of these in an efficient way. However, more importantly, is that if you take these detectors to high altitudes, the composition of the flux dramatically changes. At about 5 km, muons are no longer the dominant source of particles that can trigger a pair of coincidence detectors. In fact, protons start to dominate from 5 km upwards. So, even though we call these muon detectors, at high altitudes, like the airplane and high altitude balloon measurements shown in Sec. 7, those are primarily proton measurements.

Accidental coincident events

: Two distinct events (like two independent gamma rays) might accidentally trigger both detectors setup in coincidence mode if they happen to occur within the coincidence time window τ . This is referred to as an accidental coincidence. This probability increases at higher count rates. Assuming that individual count rates follow Poisson statistics and that the events are independent, the probability of observing n events when the mean number of events expected is μ , is described by the Poisson distribution:

$$f(n, \mu) = \frac{\mu^n e^{-\mu}}{n!} \quad (6.1)$$

Let's assume you turned on both detectors and measured the individual master count rates: N_1 and N_2 . We will now calculate the rate at which two events happen to occur within a time window τ .

The probability that Detector 2 gives no signal in the time interval τ is:

$$f(0, N_2\tau) = e^{-N_2\tau} \quad (6.2)$$

Correspondingly, the chance of getting an uncorrelated count in this window is $1 - f(0, N_2\tau)$:

$$P = 1 - e^{-N_2\tau} \quad (6.3)$$

Since normally $N_2\tau \ll 1$, we can Taylor expand:

$$P \simeq -N_2\tau \quad (6.4)$$

This is the probability of Detector 2 observing a count in time window τ . The rate of which the time window τ is opened is N_1 (Detector 1 trigger rate). Therefore, the rate at which Detector 2 observes a count in coincidence with Detector 1 is:

$$R_2 = N_1 N_2 \tau \quad (6.5)$$

Finally, Detector 2 can also have a signal before Detector 1 within the resolving time of the coincidence circuit, **the total accidental coincidence rate is:**

$$R_{acc} = 2N_1 N_2 \tau \quad (6.6)$$

For example: the average count rate for both detectors at sea level is approximately 3 Hz, and given a coincident time window of roughly $3\mu s$, we expect the mean number of events in the time window to be 9×10^{-9} ($N_{1,2} \times \tau$). Therefore, the probability of observing zero events in the time window is $f(0, 9 \times 10^{-6})$, and the probability of one detector observing an event in the coincident time window is $1 - f(0, 9 \times 10^{-6})$. Since the second detector could have also triggered first, the rate of accidental triggers is given by: $R_{acc} = 2N_1 N_2 \tau$ (Eq. 6.3.1). This corresponds to an accidental coincident rate of $54 \mu\text{Hz}$ for two detectors, or equivalently of 1 every 55,555 events, or roughly one to two events per day using two detectors, at sea level with common background levels.

But, what happens at 60,000 feet, when both detectors trigger at 60 Hz? The accidental rate is 0.02 Hz! Much higher.

Chapter 7

TESTED MEASUREMENTS YOU CAN CHOOSE FROM

You will design your own experiment for this laboratory class. The list below are some measurements that can be done at home, the lab, or office. Feel free to choose from this list or develop your own idea! Inspiration for new ideas may come from measurements described in Sec. 9.



Figure 7.1: This figure gives you an overview of the scope of the muon detectors. Some of these measurements will be described below, other we are still working on.

7.1 Cosmic-ray Muon Angular Distribution

This measurement illustrates the cosmic-ray muon angular dependence measured near sea level (it was performed in Madison, WI, at 266 m above sea level) and was previously described in Ref. [48]. Here, two detectors were set to coincidence mode and placed side-by-side as in configuration (a) of Fig. 6.3, spaced 52 mm apart, inside their aluminum enclosures. The distance was chosen such that we gain sufficient statistics throughout a single day. If the detectors are placed too far apart, the count rate drops significantly, and accidental coincidences can dominate the signal.

The angle of the detectors was determined by securing the detectors to a 100 cm long rectangular bar and then positioning the bar against a wall at a known height (see Fig. 7.2 (right)). It is important when making this measurement that the angle of the detectors is accurately measured. Fig. 7.2 (left) shows the measured relative rate as a function of zenith angle (with zero radians representing vertical). Each data point represents approximately 10 hours of data, and the rate uncertainties are statistical. The horizontal (x-axis) uncertainties represent the calculated opening angle of the two detectors when spaced 52 mm apart. The measurement at $\theta = \pi/2$ is divided by 2, since at this angle it accepts cosmic-ray muons from both directions, whereas all the other angles only accept down-going muons.

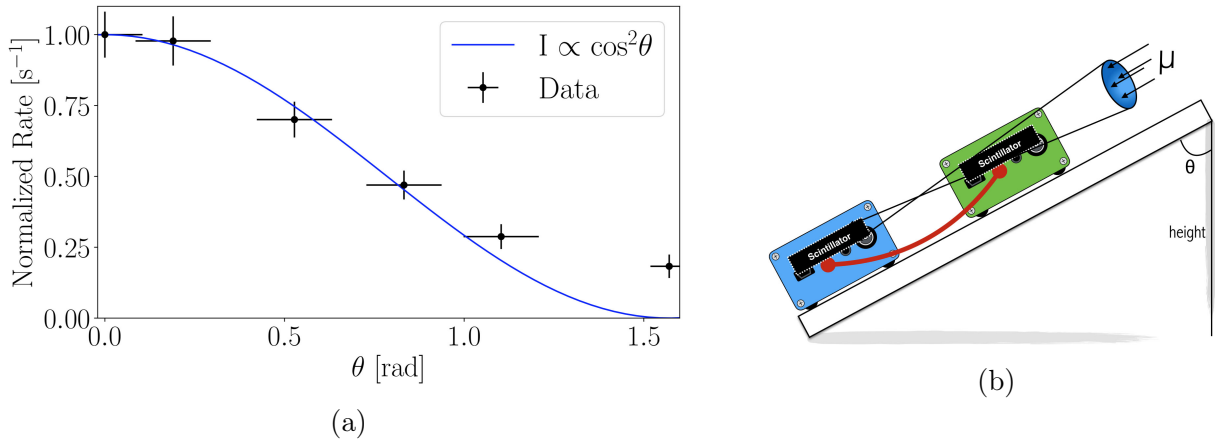


Figure 7.2: The measured cosmic-ray muon angular distribution measured by the coincident detector. The prediction by the PDG is shown in solid blue. From Ref. [48].

As indicated in Sec. 2.1.2, the angular cosmic-ray muon dependence at sea level should follow a cosine squared dependence. The overall measured shape of the distribution is found to agree relatively well with the cosine squared prediction; however, it is shown that the rate does not fall completely to zero in the horizontal configuration ($\theta = \pi/2$). This anomaly appears to be related to showers of particles developing in the roof above the detector, producing a spray of high-energy electrons or photons that can trigger both detectors. Further investigation can be conducted by shielding one of the detectors with a dense material (such as lead or iron) and performing the horizontal measurement a second time. Additionally, doing the measurement near a basement wall can provide additional shielding.

7.2 Cosmic-ray muon attenuation in a Subway station

While visiting the Research Center for Neutrino Science (RCNS) at Tohoku University, we noticed that the Aobayama subway station was extremely deep underground and decided to investigate if there was a noticeable change in the muon rate compared to the office where we was working. After spending approximately 30 minutes in the station, we decided to travel to another station (Aoba-Dori Ichibancho station) a bit closer to my hotel to see if the rate changed, and then took a final measurement at ground level.

The muon attenuation was found to be surprisingly pronounced, as shown in Fig. 7.3. We would anticipate this measurement also working rather well in the deep subway stations. Are there any deep subway stations nearby? Washington Park station in Oregon is the deepest at 79m. Forest Glen station in DC is apparently pretty deep as well. If you measured the rate as a function of depth, you could reverse this, and use the detectors to tell you how far underground you are. This is a measurement of what we call overburden. It's often reported in meter-water-equivalent, which corresponds to the amount of water overhead that would be needed to have the same shielding effect.

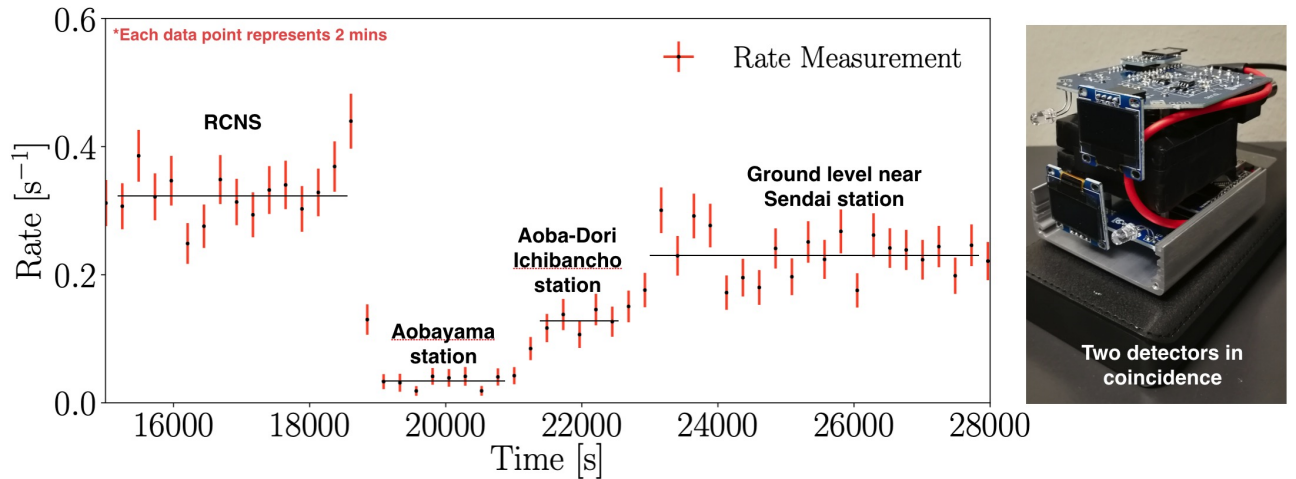


Figure 7.3: Subway in Japan.

There are likely other underground areas in your area from which this measurement can be made. While the cosmic ray muon flux per unit solid angle is from directly above, the largest flux, per unit zenith angle, is actually near 70 degrees. To get a good measurement, you must not only consider the vertical overburden but also the overburden away from vertical.

7.3 Electromagnetic component of cosmic-ray showers

We've explored in Sec. 2.1 that at sea level, there exists a flux of electrons and positrons showering down on the Earth. The majority of this flux possesses energies less than 100 MeV, with a minimal contribution above 1 GeV. Subsequently, in Sec. 3.2, we delved into the fact that this electromagnetic component is not particularly penetrating and can be significantly attenuated with a few tens of centimeters of concrete (the radiation length in concrete, as found in Table 3.1, is 10.7 cm). To test this assertion, we can measure the coincidence rate on top of a building and then again several floors lower.

We anticipate minimal attenuation of cosmic ray muons, but a significant reduction in the electromagnetic component. A typical building often features around 15 cm of concrete between each floor. By measuring the vertical muon rate on the top floor and then repeating the measurement 5 floors lower, we expect the electromagnetic component's energy to be attenuated by 7 radiation lengths (a factor of 1000).

Two detectors were placed in coincidence mode, one atop the other, following configuration (c) of Fig. 6.3. They were positioned on the rooftop of the 10-floor WiPAC building for a 24-hour period, enclosed in a plastic bag for weather protection. Subsequently, the same two detectors were relocated to the 5th floor, and the measurement was reiterated. The outcomes of this measurement are presented in Fig. 7.4.

The results reveal that the rate on the building's top floor is 27% higher than the measurement made on the 5th floor. This discrepancy in rate is presumed to be primarily attributed to the reduction of the electromagnetic component. As elucidated in Sec. 2.1, we elucidate that approximately 33% of the total cosmic ionizing radiation flux at sea level emanates from the electromagnetic component.

We've always entertained the idea of conducting a study by submerging CosmicWatch into a lake. In such a scenario, the level of shielding is precisely defined and is commonly expressed in physics experiments in terms of meter water equivalent (m.w.e.). If you decide to embark on this experiment, ensure that your detectors are enclosed in a water-tight container. An anticipated 30% reduction in the coincident rate is expected within the initial few feet as the electromagnetic component diminishes. Following that, there will be a more gradual decline in the muonic component as you proceed deeper into the water, ideally reaching depths of tens of meters.

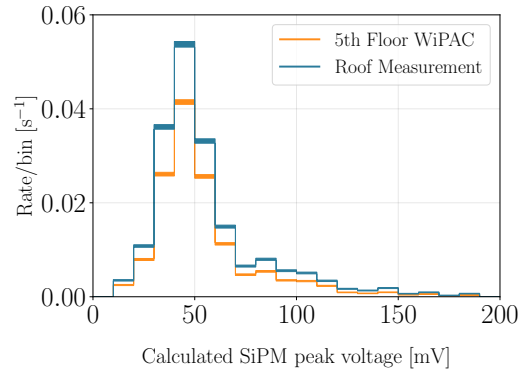


Figure 7.4: The calculated SiPM peak voltage on the roof of the WiPAC building compared to on the 5th floor.

7.4 Reducing radioactive backgrounds

There is a notable presence of natural radioactivity in the environment that the CosmicWatch detector can detect. Certain items, such as orange FiestaWare plates from 1936-1943 used natural uranium for coloring, exhibit radioactivity (Prof. Axani has a few if you are interested in seeing them). Even common household items like potassium chloride (salt substitute) can produce a signal (requiring approximately 11 oz for detection). Additionally, granite countertops in homes might also exhibit radioactivity, so it's worth checking for.

Shielding against natural radioactivity in the environment can be challenging. Typically, at sea level, the largest component of our signal originates from radioactive backgrounds. Therefore, it is beneficial to explore ways to minimize this background and enhance the purity of the cosmic-ray muon signal (beyond using coincidence mode).

The use of dense materials around the detector can attenuate the incoming flux from background radiation. While an ideal choice would be a radio-pure material, we can illustrate the effect using lead bricks. Six lead ingots (each measuring $2'' \times 4'' \times 8''$) were strategically placed to provide 4π coverage around a single detector. The detector recorded data directly to the microSD card over the course of a full day. Subsequently, it was positioned on a workbench in the same room (far away from the lead) to measure the background spectrum for another full day. The resulting calculated SiPM peak voltage for the two measurements is depicted in Fig. 7.5. As anticipated, this setup significantly reduces events contributing to the low SiPM peak voltage region, which is predominantly influenced by radioactive background.

Lab 303 (AxLab) has several led bricks if you would like to use them. Alternatively, you can experiment with different materials, bury the detectors in the ground, or try using water (ensuring the detectors are sealed securely). Explore measuring the effectiveness of various materials of the same thickness and consider why some materials are more effective than others. Additionally, investigate the impact of different thicknesses of shielding.

Another experiment you can conduct involves studying the reduction in rate with distance from a radioactive gamma-ray source. To set up this experiment, you can contact a lab instructors, who have access to radioactive button sources located in Sharp Lab 016A. This experiment provides an opportunity to demonstrate the inverse square law ($1/r^2$) decay associated with ALARA (As Low As Reasonably Achievable) principles, a concept emphasized in radiation safety lectures.

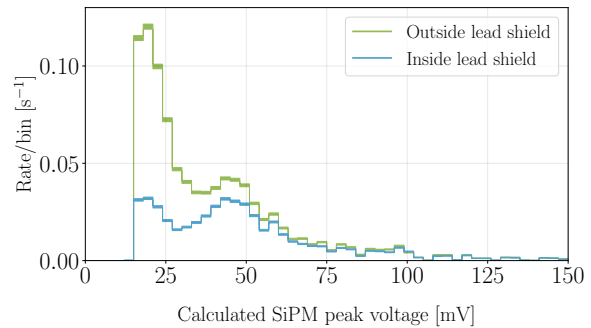


Figure 7.5: The effect of surrounding a single detector in a lead enclosure.

7.5 Correlation between the cosmic-ray muon rate and atmospheric pressure

A correlation exists between the atmospheric pressure and the cosmic-ray muon rate. It can be expressed as follows:

$$\frac{\Delta I}{\bar{I}} = \beta \Delta P, \quad (7.1)$$

where I represents cosmic-ray muon intensity, ΔP is the measured atmospheric pressure compared to the average pressure, and β is the barometric coefficient [49]. This correlation is actually the result of several processes outlined in Sec. 2.1.2. The barometric coefficient represents the percent change in detector count rate per hPa change in atmospheric pressure.

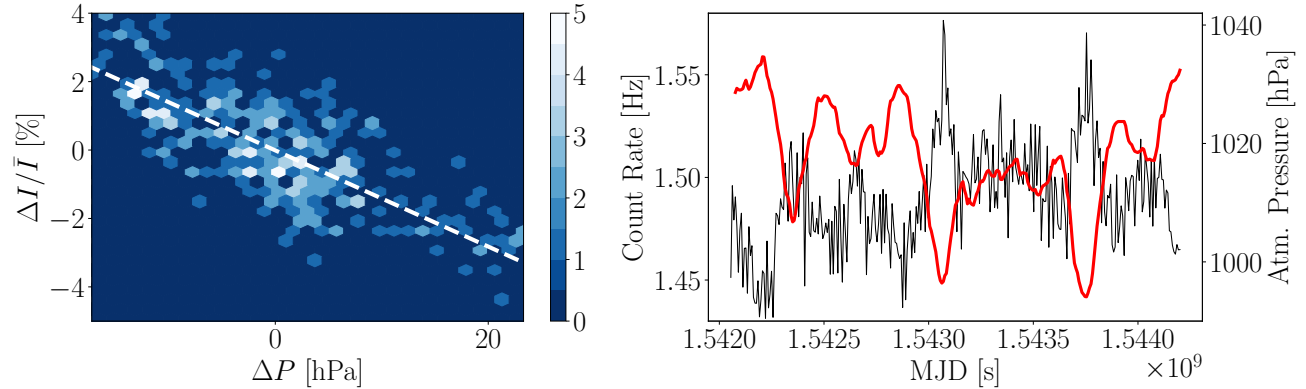


Figure 7.6: Left: The correlation between the atmospheric pressure and the detector count rate. Right: The detector count rate in blue and the atmospheric pressure in red as a function of modified Julian date (MJD). Both plots show the data binned with a bin size of two hours.

For this measurement, we decided to use an array of master-coincident detectors (ten detectors) to improve the statistics. Five pairs of detectors were each connected in configuration (c) of Fig. 6.3, and left to record the cosmic-ray muon rate over the course of 24.8 days (from 13:35 hrs Nov. 12th to 09:00 hrs Dec. 7th 2018.). Data was recorded directly to a microSD card and powered through an 8-way USB hub powered through a wall outlet. Since the CosmicWatch does not keep accurate time over long time-scales, we assume the time drifts linearly with time, and scale the uptime of all detectors such that they are all the same. This is not ideal, and we would recommend recording the data directly to a computer through the `import_data.py` script in the future to get an accurate time stamp on all events. However, this is more prone to losing data, since you would require a computer that runs continuously for a significant amount of time. The array of detectors was placed in the 4th floor WiPAC lab in Madison, WI. Atmospheric pressure for Madison was found in Ref. [50]. However, the UD version has a built in pressure sensor if you would like to try using it.

Fig. 7.6 (left) shows the correlation between the detector count rate and the atmospheric pres-

sure. The calculated correlation is shown in the dotted white line. A least squares fit yielded a barometric coefficient of -0.141 ± 0.007 %/hPa, in agreement with Ref. [51].

This may be difficult to do with only two detectors since the statistics will be lower, but it will be interesting to see! You can increase the amount of data you have if you ask a friend to also take data at their location, and you add that to yours.

One of our latest adventures is HurricaneWatch. A meteorology student who is a hurricane-chaser is taking our detectors into the storms she studies. The atmospheric pressure during a hurricane can drop by over 100 hPa, which we hope to be able to see. We will be excited to get this dataset!

7.6 A true random number generator?

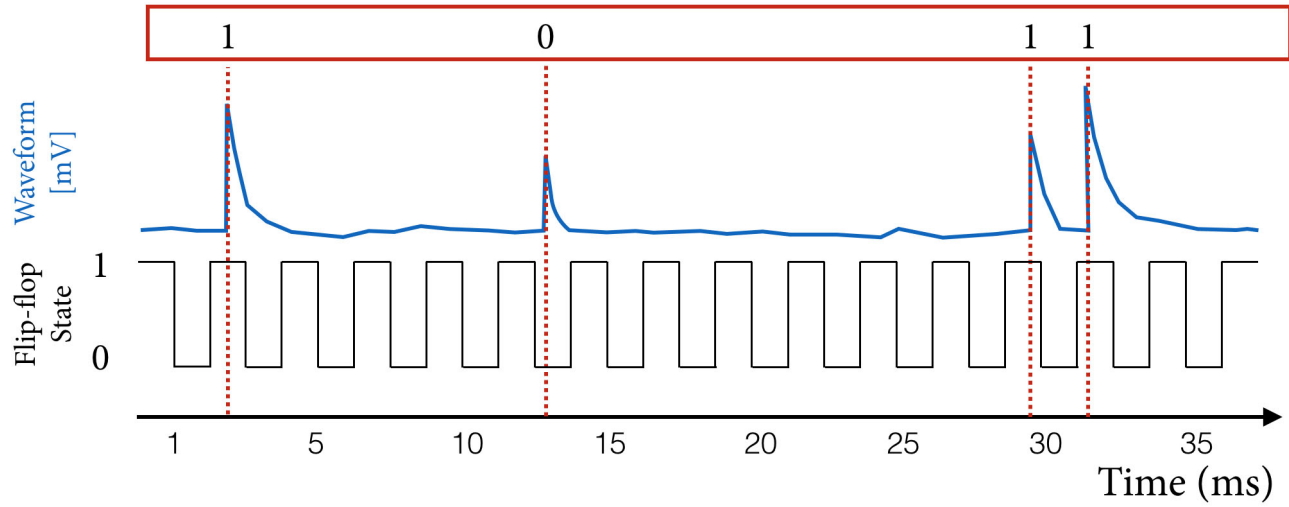


Figure 7.7: An illustrative diagram of the principle behind the random number generator. The x-axis indicates the time measure in milliseconds. Above this, we have the toggle flip-flop, which changes state every millisecond, then an illustrative waveform shown in blue. If the event triggered the detector while in the even state of the flip flop, we assign it a one, otherwise, we assign it a zero. This is shown in the red box at the top of the diagram.

Many applications require random numbers. Often, a random number may be generated through some algorithm, but this, therefore, becomes deterministic since if the user knew the algorithm and starting conditions, they could determine the output. An ideal random number generator would be derived from a truly random process, such as the arrival times of cosmic-ray muons or the radioactive decay of an element. The sum of two random processes will also be random, such as the signal from the radioactive backgrounds in the detector along with the cosmic-ray muon signal. For this measurement, we are following the description found in Ref. [8].

Any number can be expressed in terms of a sequence of ones and zeros; this is known as binary. An N -length sequence is able to represent a number from zero to $2^N - 1$ (corresponding to 2^N different values). For example, the 4-bit binary sequence "1011" corresponds to $1 \times (2^3) + 0 \times (2^2) + 1 \times (2^1) + 1 \times (2^0) = 8 + 0 + 2 + 1 = 11$.

We can convert the time stamp of a radioactive decay trigger into a "1" or a "0" using a *toggle flip-flop*. The toggle flip-flop is simply a state that changes from one to zero periodically (we will use a frequency of 1 kHz). If a particle passes through the scintillator during an even time stamp (as measured in milliseconds), we assign it a "1"; if it passes through an odd time stamp, we assign it a "0". After N triggers, we can build an N -bit random number. This is schematically illustrated in Fig. 7.7.

For this measurement, we use data taken from a 20-day background lab measurement. A single

detector was used. After triggering on a total of t events, we can build t/N N-bit random numbers. To illustrate this, if we choose to generate 8-bit random numbers (from 0 to 255), we can plot the number of each occurrence. This is shown in Fig. 7.8.

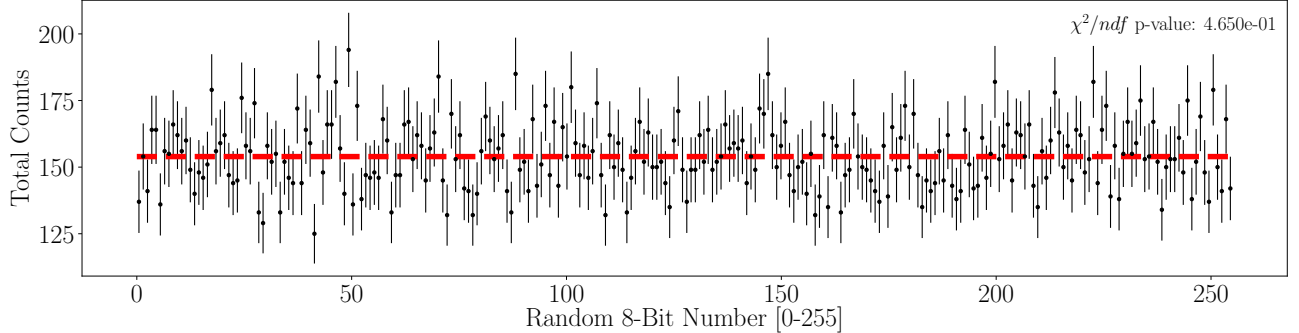


Figure 7.8: The number of occurrences of the generated numbers from 0-255. The reduced χ^2 p-value assuming that the distribution should be randomly distributed about the average number of occurrences is given at the top right of the figure.

Fig. 7.8 shows the random nature of the triggers. Each number should be equally probable to occur. The reduced χ^2 indicates a p-value for this assumption shown in the top right of the plot.

In your case, you may consider collecting data from a natural radioactive source. A suitable option is to acquire an 11 oz or larger container of salt substitute (potassium chloride) for this study. The radioactive emissions from the potassium chloride will contribute to a count rate that is higher than the background when the source is placed near the detector.

There are several factors that can introduce bias into the random number generator. Let's consider extreme scenarios. Imagine a scenario where the trigger rate is approximately 1 Hz, and the flip-flop state changes only every 10 seconds. In this case, the first ten triggers would yield all ones, followed by the next ten triggers giving all zeroes. This would result in biased high values for the initial numbers and biased low values for the subsequent ones. This example highlights the need for the toggle flip-flop to change states at a much higher rate than the trigger rate.

Another potential source of bias arises if the microcontroller fails to produce an equal number of even and odd timestamps due to internal configuration issues. For instance, when using



Figure 7.9: Background rate measurement with (left) and without (right) an 11 oz container of potassium chloride. The rates are measured as 7.2 ± 0.1 Hz and 3.94 ± 0.08 Hz, respectively.

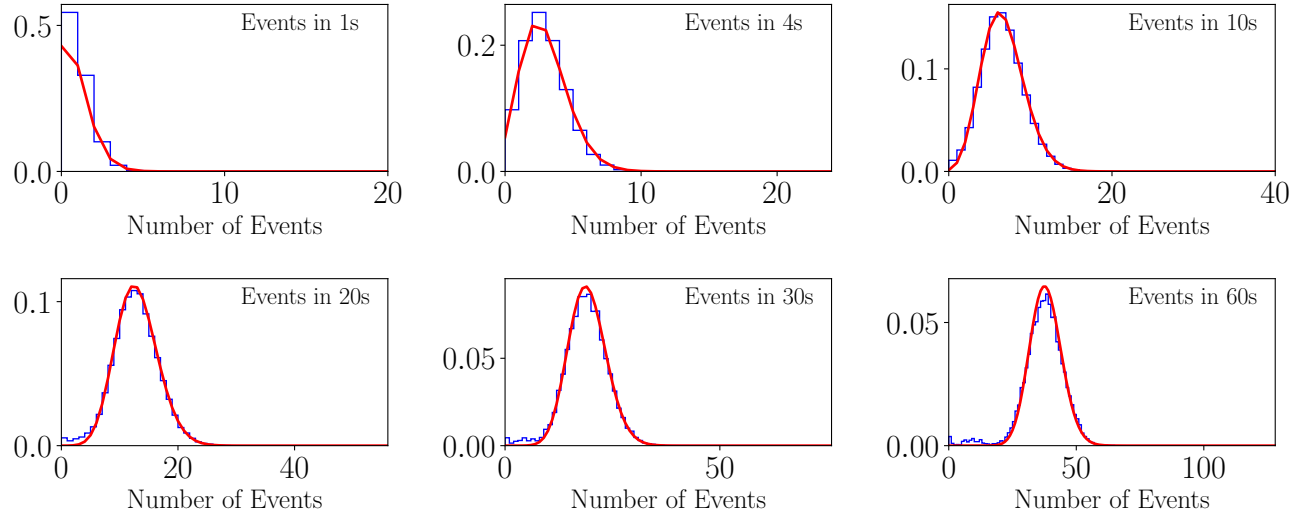


Figure 7.10: The distribution of number of events per unit time. Each cell represents a different amount of time in which the data is binned (labelled on the top right of each cell). The red line is the expected Poissonian distribution from Eq. 6.3.1.

the microseconds() function in Teensy/Arduino, the reported timestamp may only be accurate to the nearest even microsecond. It is crucial to thoroughly study and quantify the randomness of the data collected.

A funny thought could be to use this idea to turn the detector into a *magic eight ball*.

7.7 Gamma-ray spectroscopy

The detection material is primarily composed of polystyrene, a low-density synthetic hydrocarbon. Referring to Fig. 3.4, we observe that for carbon-based materials, at MeV gamma ray energies, the predominant interaction is Compton scattering. Ideally, in gamma ray spectroscopy, capturing the full energy of the gamma ray, as in photoelectric absorption (more common in high-density materials like germanium), is desired. However, in our case, a common interaction involves the original gamma ray undergoing Compton scattering within the scintillator, depositing some energy, and then leaving the scintillator. This results in a smeared energy distribution, lower mono-energetic peaks, and an increased rate in the Compton valley.

While challenging, some information can still be extracted from gamma ray sources, as exemplified in Fig. 7.11. In this context, data was collected with various sources at the MIT Junior Lab. Although we may not be able to discern monoenergetic peaks, interesting features emerge. For instance, Cobalt-60 emits two relatively high-energy gamma rays (1.17 and 1.33 MeV) compared to Cesium-137, which features a dominant gamma ray at 0.66 MeV. It is worth noting that the SiPM peak voltages, serving as a proxy for the number of observed photons and related to the energy deposited by a gamma ray, exhibit variations.

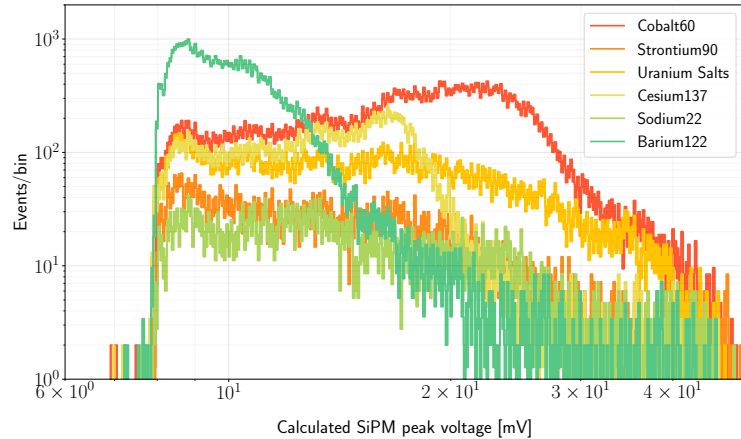


Figure 7.11: The distribution of number of events per unit time. Each cell represents a different amount of time in which the data is binned (labelled on the top right of each cell). The red line is the expected Poissonian distribution from Eq. 6.3.1.

Gamma ray spectroscopy with these detectors would be enhanced by utilizing a denser material, larger volume detectors, and greater photocathode coverage. We do have dense scintillator crystals if you would like to try.

Chapter 8

UNTESTED MEASUREMENTS FOR THE ADVENTUROUS

This section outlines a selection of measurements that we aspire to include in the curriculum in the near future. Opting for one of these measurements means venturing into relatively unexplored territories. We highlight the challenges associated with these measurements, and in the case of the solar flare measurement, success depends on fortuitous timing! Therefore, exercise caution. Nonetheless, if you successfully conduct any of these measurements, they could potentially become part of next year's curriculum! Best of luck!

8.1 The velocity of cosmic-ray muons

To reach sea level, cosmic ray muons must travel at relativistic speeds. One way to measure their velocity involves assessing the time delay between their passage through two widely separated scintillation counters.

While the CosmicWatch detectors have a triggering electronics precision in the order of microseconds, limiting the observable travel time differences to distances requiring thousands of feet between detectors, there is a potential approach using an Oscilloscope. By accessing the output of the SiPM inside the detector, you can obtain a signal with a fast rise time. Placing two detectors several feet apart and digitizing both fast outputs using the Oscilloscope might reveal an observable shift.

However, this measurement is challenging due to the limited statistics. To detect a shift of 1ns, the detectors would need to be approximately 1 feet apart. Can you detect a 1ns shift? It might require you to fit the SiPM curve to the digitized waveform to get an accurate time stamp. You could separate them by, say, 12 feet, but you will have small statistics. Could you estimate the rate? At such distances, the coincident rate is low, very low, and the accidental coincidence rate requires careful investigation.

Before attempting this measurement, consider the method you plan to use for recording data. Ideally, you would want the Oscilloscope to save the waveform of all observed coincident events for offline analysis. To assess the feasibility of your setup, you could start by using two BNC cables of different lengths, e.g., 6" and 8". The observable signal travel time difference between these cables, in a coincident event with detectors placed close together, will provide insight into the required detector separation to observe a difference given the Oscilloscope's limited sampling speed. During the actual measurement, ensure that the BNC cable lengths are the same.

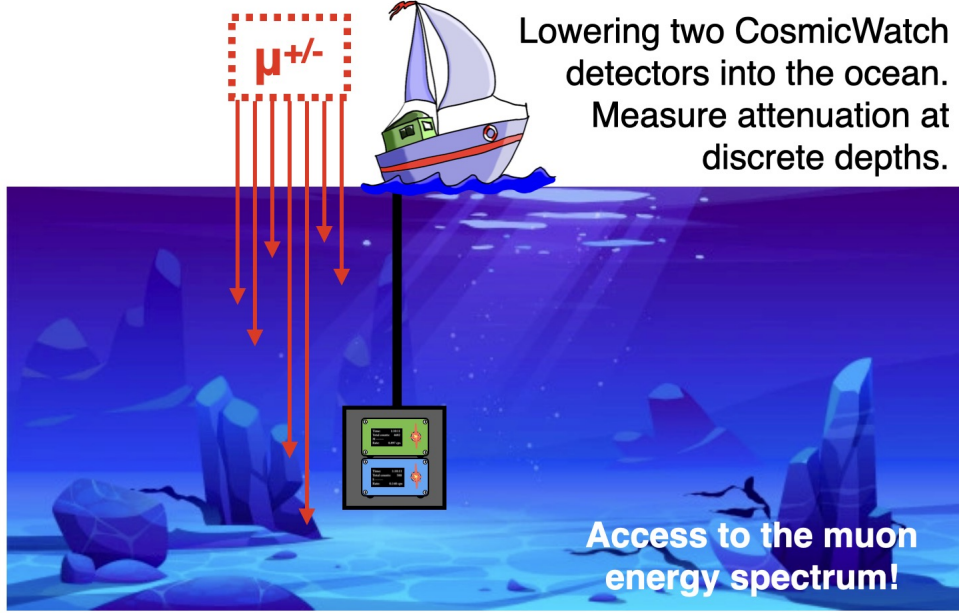


Figure 8.1: Measuring the muon rate as a function of depth underwater should be able to give you the muon rate.

8.2 Muon Rate Underwater

Physicists typically report the equivalent overburden in terms of how much water would provide the equivalent shielding. A measurement in actual water can be useful since it provides a homogeneous material and is abundant. We will attempt to measure the attenuation as a function of depth in a deep lake/ocean. Initially, we should observe a steep decrease due to the electromagnetic component dropping out, then a slow decrease as a function of depth. If you frequent a pool, they may let you take data in the deep end. A student at MIT dropped them in the Charles River to measure the attenuation.

It's neat actually. If you could measure how the rate decreases with depth, you should be able to extract the muon energy spectrum. That is, if muons had extremely high energies, they would penetrate deeper into the water. This would be a tricky bit of unfolding, but extremely cool.

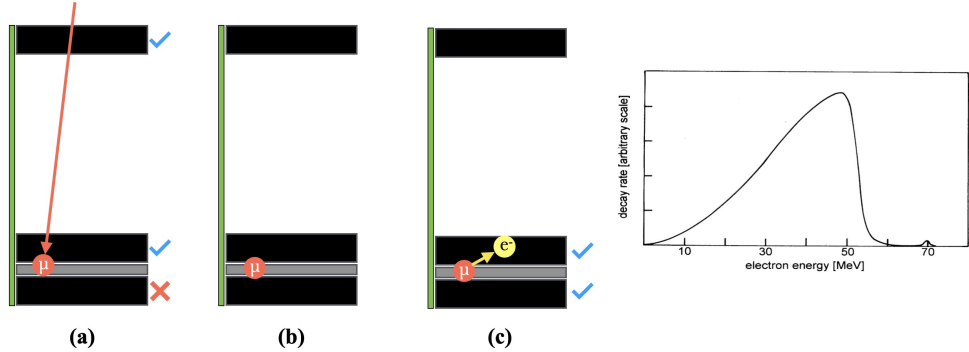


Figure 8.2: (a) A muon passes through the top and middle detector. (b) It hangs out for a bit. (c) the second or third detector observe something 100s of ns to a few microseconds later, as the muon decays to a Michel electron.

8.3 Muon lifetime

This is cool. It might be possible to measure the lifetime of the muon. As mentioned earlier in this document, the muon is unstable. Their rest mass is approximately $207 m_e$. It has a lifetime of roughly $2.2 \mu s$. The fact that muons are sufficiently energetic and decay only under the weak interactions causes that they can reach sea level. When it decays, it emits two neutrinos (invisible to us), and a fairly energetic electron, called the Michel electron. The Michel electron energy spectrum is shown in Fig. 8.2 right. If you can stop a muon and see how long it hangs around for, you can get the muon lifetime. I think you will need three detectors though. We have a special detector in Lab 303 that might be suitable for this. It's shown in the image below, Fig. 8.2.

With three detectors one-on-top of each other, this measurement should be possible. The top two are used to trigger on an incoming muon. If the bottom detector doesn't trigger, that likely means that the muon stopped in the middle detector. Then you wait. Not long though, since after a few 100s of nanoseconds, the Michel electron should pop out and trigger either the middle or bottom detector. By measuring the time it takes between these two signals, you can infer the muon lifetime by fitting an exponential + constant to the Δt time between trigger and the Michel. The exponential decay constant represents the lifetime of the muon. The constant is there to account for the accidental coincidences, which are independent and therefore will have a constant rate.

8.4 Solar flares and the Forbush decrease

At higher altitudes and latitudes, where lower-energy primary cosmic ray particles are observable, a correlation between cosmic radiation and solar activity becomes apparent. Solar flares, often associated with coronal mass ejections, can lead to significant temporary increases in count rates. This effect is more pronounced at higher altitudes, where the Earth's magnetic field offers less protection to GeV cosmic ray particles compared to regions near the equator.

NASA and the National Oceanic and Atmospheric Administration operate the Geostationary Operational Environmental Satellite (GOES), which records the incident particle flux from the sun, including protons, electrons, and X-rays. Publicly available data from GOES can be used to correlate transient solar events with cosmic ray muons. Solar flares are classified using letters A, B, C, M, or X, representing the power per unit area of an event. A numerical suffix (0 to 9) indicates the event's strength; for example, an X2 flare has twice the strength of an X1 flare. Each letter classifies events with an order of magnitude difference between classes, with X denoting the most powerful flare classification. While X-class solar flares are relatively rare, occurring only a few times per year, there's a chance your detector might be active during such an event!

The real-time clock on CosmicWatch detectors is updated each time the software is re-uploaded to the Teensy 4.0. Over time, clock drift may occur, leading to an inaccurate local time stamp. However, this might not be a significant issue since solar flares can have relatively long durations. If clock drift is a concern, data can be recorded directly to the computer, where the computer's time stamp is replaced with the RTC time stamp, providing a more accurate reading.

Roughly one day after a solar eruption, the Earth undergoes a solar storm. A brief increase in the magnetic field is observed, followed by a much more pronounced decrease that persists for several hours. Over the span of a few days, the magnetic field gradually returns to its initial strength. This phenomenon is known as the "Forbush decrease." Initially, the observed cosmic ray radiation intensity starts to decrease.

Given the crucial role of Earth's magnetic field in shielding us from cosmic radiation, this effect should also be observable. As illustrated in Fig. 8.3, the change in rate is at the percent level. Changes at the percent level should be detectable over the course of a day using configuration (d) of Fig. 6.3. However, it's important to note that atmospheric conditions may also influence the measurement, so considering barometric pressure measurements could be beneficial.

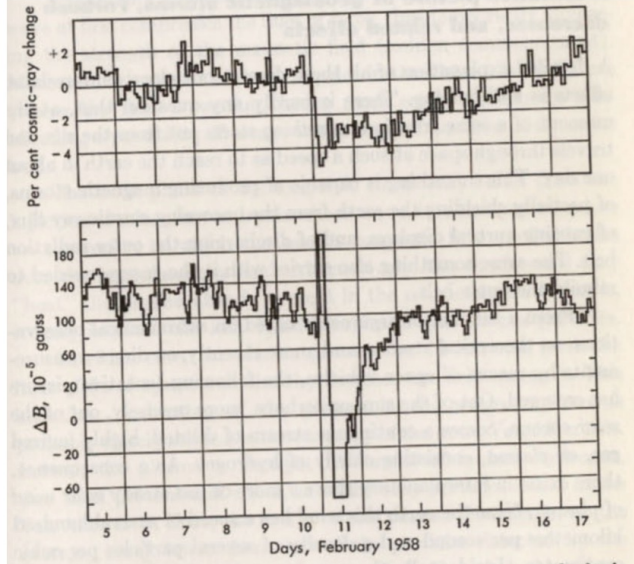


Fig. 14-2 Typical Forbush decrease. The lower curve represents the horizontal component ΔB of the magnetic field measured, from an arbitrary zero, in units of 10^{-6} gauss. The upper curve shows the corresponding variations of cosmic-ray intensity (measured by a neutron monitor in Chicago) as a percentage of the normal intensity. Shown on the horizontal axis is the universal time, in days. (From F. Bachelet, P. Balata, A. M. Conforto, and G. Marini, *Il Nuovo Cimento*, vol. 16, p. 292, 1960.)

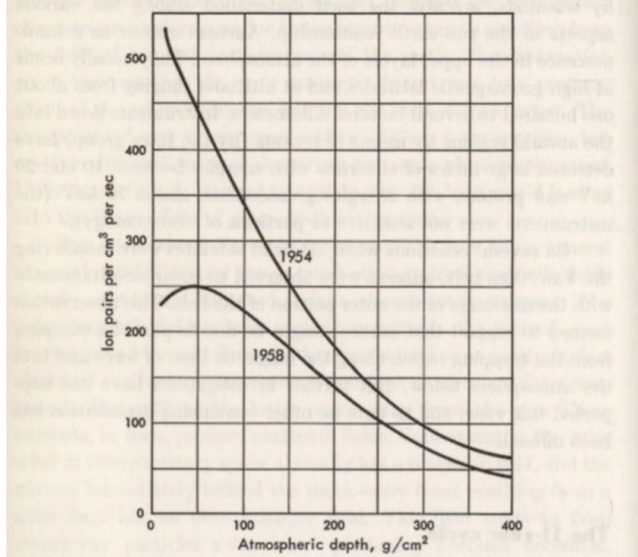


Fig. 14-3 Intensity of cosmic rays as a function of atmospheric depth, measured at a geomagnetic latitude of 88° N at the time of minimum solar activity in 1954 and at the time of maximum solar activity in 1958. The instrument used was an electroscope; the vertical scale gives the number of ion pairs per second produced by cosmic rays in 1 cm^3 of air at standard temperature and pressure. The horizontal scale gives the atmospheric depth, in grams per square centimeter. (From H. V. Neher, *Nature*, vol. 184, p. 423, 1959.)

Figure 8.3: The Forbush decrease (left) and solar maximum/minimum cosmic-ray flux (right). This figure comes from Ref. [3].

8.5 Measuring the air shower size

Air showers were first discovered using coincidence counters, a concept very similar to the one employed in CosmicWatch. An air shower involves multiple particles arriving simultaneously. Such showers can occur when muons interact while traversing material above the detector, such as the building's roof, or, as depicted in Fig. 8.4, a sheet of lead.

The objective of this measurement is to investigate coincident events between two sets of coincidence detectors based on the lateral distance between the two sets. The challenge lies in the potential requirement for 3 to 4 detectors, as illustrated in Fig. 8.4. Two sets of coincidence detectors (totaling 4 detectors) would yield a lower accidental coincidence rate compared to using 3 detectors (excluding detector C). While the detectors are not configured to record triple coincidences via the microSD card, connecting all detectors to a single computer (via a USB hub) allows the data from each detector to be saved in a unified file using the `import_data.py` script. The timestamps from the computer data can then be analyzed to identify coincidence events.

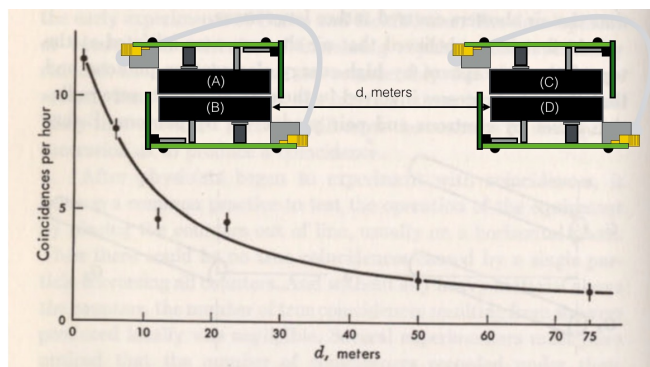


Figure 8.4: Recommended configuration for measuring air shower size. Data from Ref. [3].

Chapter 9

FUN MEASUREMENTS WE HAVE DONE

You will not be able to do the set of measurements we describe here. However, they are fun to read about. And they may inspire ideas so you can make some fun measurements too!

9.1 Measuring the cosmic-ray muon rate in an airplane at 33,000 ft

A rate measurement was conducted during a flight from Boston International Logan Airport (BOS, latitude = 42.4°) to Chicago O'Hare Airport (ORD, latitude = 42.0°) using a single detector. The data was recorded onto a microSD card and powered by a 10,000 mAh USB power bank. The altitude of the airplane was obtained from flight records available on FlightAware.com [52].

Fig. 9.1 (left) illustrates the detector's trigger rate in blue as a function of time, binned into 60-second intervals. The error bars depicted are solely statistical. Airplane altitude data were linearly interpolated between points to estimate the altitude at any given minute. The interpolated altitude data were fitted to the detector data using a simple exponential plus an offset. Since the absolute take-off time was unknown (data recorded to the microSD card), we allowed the altitude timestamps to shift during minimization. The best-fit equation is displayed at the top left of this figure, where $\text{ALT}[t]$ represents altitude measured in kilometers as a function of time. The best-fit is also presented as a dashed red line.

Fig. 9.1 (right) displays the measured trigger rate as a function of true altitude. Here, we extend the exponential fit beyond the measured values. The count rate uncertainties were calculated by taking the square root of the sum of all events measured at a particular altitude. It's important to note that this data was collected with a detector in master mode, making it sensitive to background radiation from the interior of the plane.

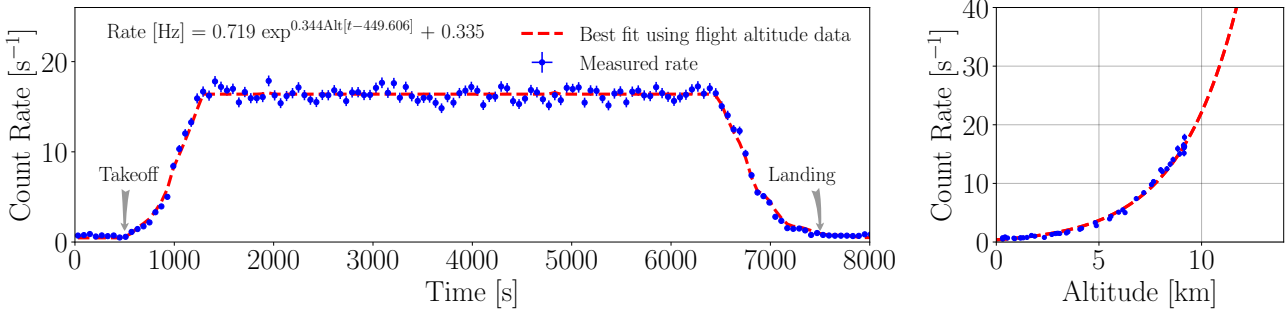


Figure 9.1: (Left) The count rate measured during a flight from Boston to Chicago as a function of flight time. The dashed red line shows the actual amplitude of the airplane [52] scaled by a fitted exponential shown at the top left of the plot. (Right) The measured count rate as a function of altitude. The dashed red line shows the fit.

The cosmic-ray muon flux is recognized to vary with latitude, a variation we have sidestepped by measuring the flux at a nearly constant latitude. Additionally, we anticipate the exponential fit to become less reliable as we extend to higher altitudes, owing to the alteration in flux composition near the primary cosmic ray interaction region.

9.2 High altitude balloon measurement at 107,000 ft



Figure 9.2: An image from the high-altitude balloon flight at 107,000 ft. Photo from *Daniel Kaczmar - DNF Systems*.

As mentioned in Sec. 2.1, primary cosmic rays interacting in the upper atmosphere produce showers of particles, some of which decay to muons. Muons are typically produced near an

altitude of 15 km. At higher altitudes, there is an increase in the contribution from other ionizing particles, primarily from electrons/positrons and protons.

During the NearSpace2018 conference [53] in Torun, Poland, we participated in a high-altitude balloon (HAB) flight to measure the ionizing radiation flux as a function of altitude. Two detectors were used for the flight, allowing measurement of both the total rate on the master detector and the down-going rate on the coincident detector. The detectors were placed one-on-top of another (configuration (d) in Fig. 6.3) and taped together to ensure their orientation relative to each other remained constant throughout the flight. The BNC connectors and the OLED screens were removed from the PCB to reduce weight. An 8" 3.5 mm audio cable was used to connect them into coincidence mode, and the SDCard.ino code was uploaded to both detectors. An image of the two detectors is shown in Fig. 9.3. Both detectors were powered by a single-cell lithium-ion battery.

The temperature during the ascent was expected to reach -60°C , requiring thermal protection for both the battery and to minimize the effect on the SiPM described in Sec. 4.1. A $10 \times 10 \times 10 \text{ cm}^3$ Styrofoam enclosure with a wall thickness of 1 cm was constructed to house the components. It was large enough to accommodate the two detectors, a small heating element, and two single-cell lithium-ion batteries (one to power the detectors and the other to power the heater). A micro-switch was connected to the battery and wired outside the enclosure so that we could initialize the detectors from outside the enclosure just before the flight.

The HAB was launched on September 22nd, 2018, at 12:53 pm. DFN System recorded the balloon altitude and location using on-board GPS, and they mounted a camera to the balloon that looked down at the payloads. An image near the maximum altitude of the flight is shown in Fig. 9.2. The master (orange) and coincident (green) detector count rate, binned into 60-second intervals, is shown in Fig. 9.4, along with the altitude data from the GPS (black).

The shape of the measured spectrum in Fig. 9.4 corresponds to the Pfotzer curve. We find an initial maximum count rate (Regener-Pfotzer maximum) for the master detector at an altitude from approximately 16-23 km, around 70-95 minutes into the measurement. After the balloon popped (at minute 118), the detectors fell through the Regener-Pfotzer maximum. The decrease in the trigger rate after passing the maximum occurs due to the detectors ascending beyond the primary interaction region.

The coincidence detector shows a flatter maximum at an altitude from approximately 12-25 km.

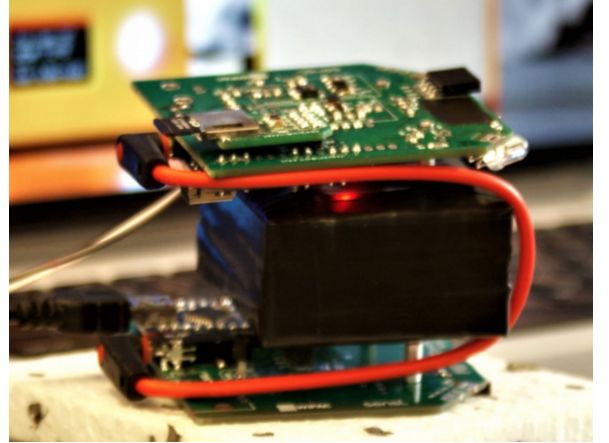


Figure 9.3: The two detectors flown in the HAB flight. The scintillators were taped together in order to preserve the detector orientation relative to each other.

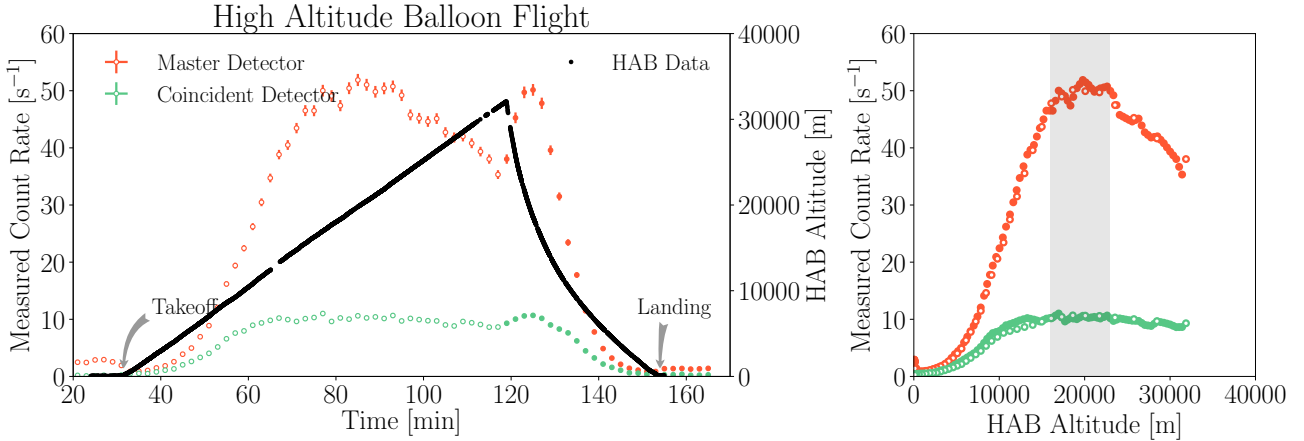


Figure 9.4: (Left) The measured trigger rate for the master (orange) and coincident (green) detector during the high-altitude balloon flight. Take-off occurred 30 minutes after powering on the detectors. The black data points correspond to the altitude as measured through the on-board GPS. (Right) The GPS altitude as a function of trigger rate. The uncertainty in both these plots are statistical.

The peak begins at lower altitudes since we are now preferentially triggering on vertically down-going particles. As described in Sec. 2.1.2, primary particles entering the Earth’s atmosphere at larger angles from the zenith will interact at higher altitudes. In agreement with the data.

9.3 Muon rate measurement while flying to the South Pole

In December 2018, I flew to the South Pole as part of a field team to perform maintenance and upgrades on the IceCube Neutrino Observatory [54]. During the flight, I measured the ionizing radiation with two detectors oriented in configuration (d) of Fig. 6.3. Data was recorded to the microSD cards and powered through a single 30,000 mAh power bank.

The first four flights (from Madison, WI USA to Christchurch, New Zealand) were operated by United Airlines and New Zealand Airlines. The altitude data was publicly available for these flights on FlightAware.com [52]. The flight leaving from Christchurch New Zealand, to McMurdo Antarctica, was on a C-17 military jet operated by the US Air Force. Similarly, we flew on a C-130 Hercules, the day after to the South Pole. Since these were military flights, the altitude of this flight was not available; however, several altitude measurements on the second flight were made using GPS. We landed several days later on the 2820 m thick South Pole glacier, approximately 0.5 km from the actual Geographical South Pole.

The full master and coincident detector data are shown in Fig. 9.6, with descriptions of each flight in the text boxes. To give perspective for other measurements, the total data collected by



Figure 9.5: Leaving McMurdo Station, Antarctica on a C-130 Hercules for the South Pole Station.

the master detector was about 50 Mb, whereas the coincidence detector was approximately 15 Mb.

Fig. 9.6 illustrates several very interesting properties. First, there is a trend towards lower count rates near the equator. This is due to the latitudinal variation in the cosmic-ray flux described in Sec. 2.1.2. This effect is most obvious in the flight from SFO to ACK (labeled as flight 3 in Fig. 9.6), which traveled at nearly a constant altitude and a constant rate of latitude change from $+32^\circ$ to -32° . We see that the rate is not symmetric. This is because the magnetic latitude is offset from the geographical latitude, which in turn is because the magnetic field is not symmetric about the equator. Second, it's interesting to see that when we landed at the South Pole, there is a noticeable change in trigger rate due to the combination of the elevation and change in Earth's magnetic field.

While flying through the equator at 35,000 ft, I also performed an East-West measurement using configuration (e) of Fig. 6.3. We measure a count rate coming from the east of 0.69 ± 0.02 cps, while from the west 0.84 ± 0.03 cps. This represents a $22.2 \pm 7.4\%$ increase in the westward direction. This is due to the east-west asymmetry described in Sec. 2.1.2.

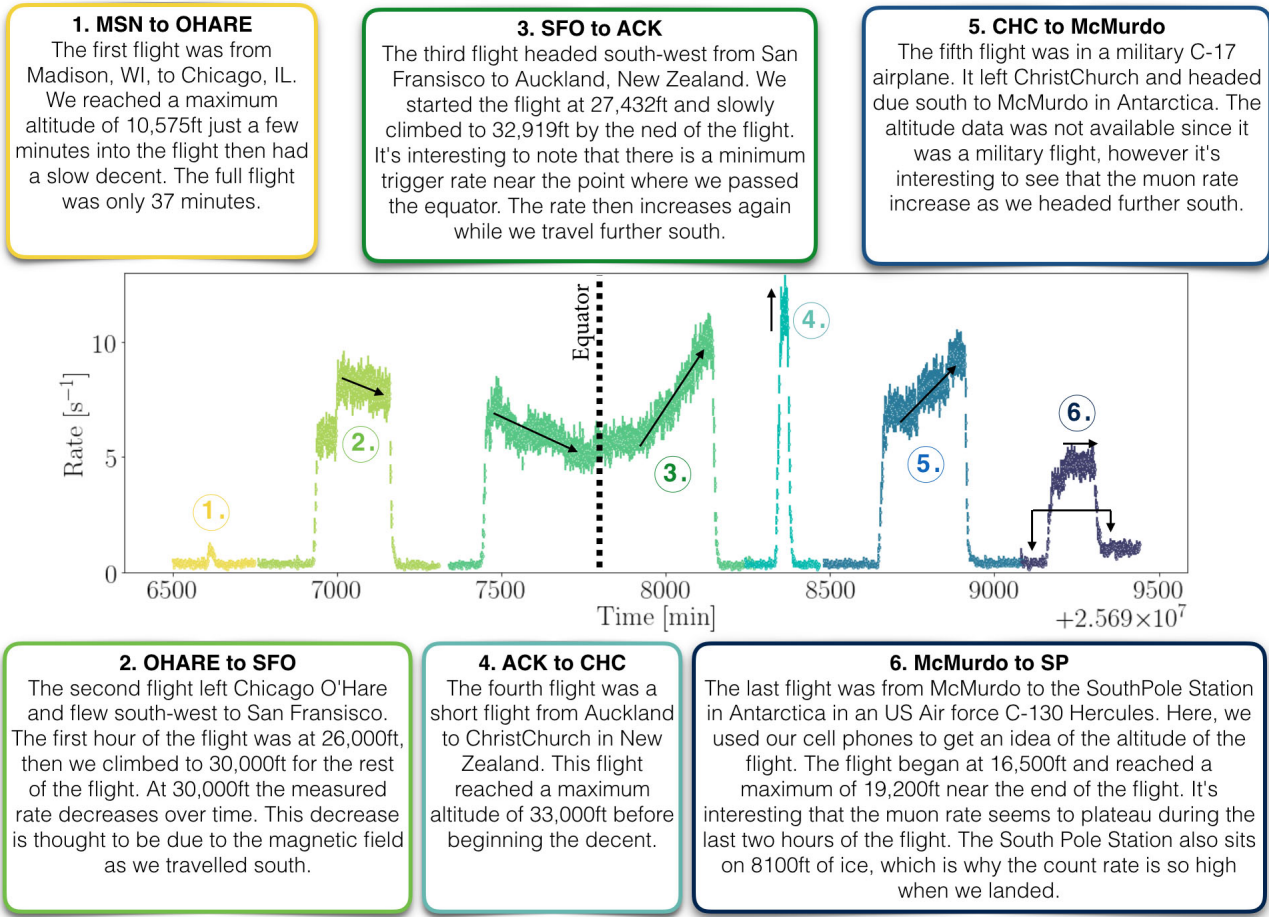


Figure 9.6

9.4 Latitude correction to the cosmic-ray muons

We observed latitudinal variation in the cosmic-ray muon rate in the previous measurements. This was an expected effect due to the change in the Earth's magnetic field as a function of latitude. Here, we will empirically attempt to account for the variation in the latitude and altitude based on the previous measurement. We will assume that the change in the rate as a function of latitude follows a sine-squared form, where the minimum occurs near the equator and the maximum occurs near the poles.

$$R[Hz] = N \exp^{\alpha(\sin(LAT[t]+\theta)^2 + \beta \times ALT[t])} - b \quad (9.1)$$

Here, θ represents a phase that offsets the latitude to account for the difference between the geographical latitude and the magnetic latitude, β is a factor that permits an altitude effect at the magnetic equator (set the sine term to zero), α is a scale factor that dictates the strength of

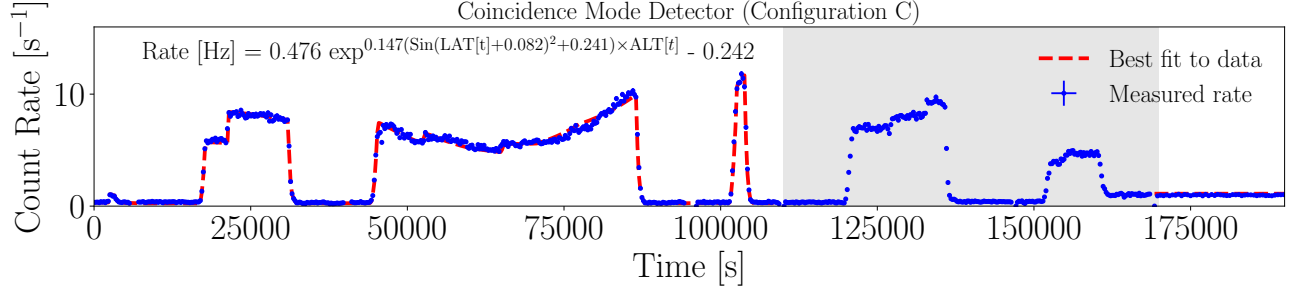


Figure 9.7: The fitted data based on the altitude and latitude data from the first four flights. The fit also includes a measurement after landing at the South Pole, where the altitude and latitude were known (2700 m and -90°). The two military flights were not included in the fit.

the latitudinal and altitude effect, N is a normalization that sets the scale for the exponential component, and b is an offset that accounts for constant background radiation.

Figure 9.9: Caption goes here.

Fig. 9.9 uses the function in Eq. 9.1 to fit the data for the first four flights, plus the data after landing at the South Pole. The best fit values are shown at the top left of Fig. 9.9. Using this result, we can then invert Eq. 9.1 to calculate the altitude of the two military flights (assuming we flew at a constant velocity directly south). The calculated altitude is shown in Fig. 9.8 for the military flights in green, as well as the measured altitude from GPS in red.

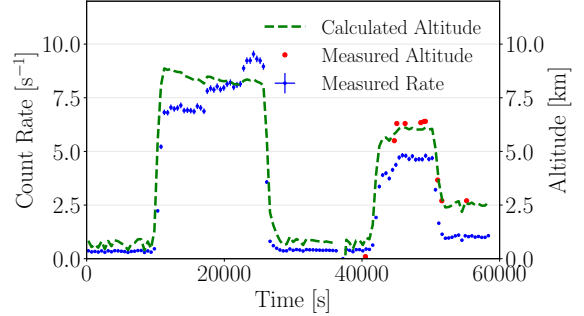


Figure 9.8: The measured muon rate in blue along with the calculated flight altitude in green. The red markers show the few GPS altitude measurements during the flight.

9.5 Rate measurement 1 km underground at Super-Kamiokande



Figure 9.10: Dr. Katarzyna Frankiewicz floating in the inner detector of Super-Kamiokande during the Gadolinium upgrade 2018.

Two Desktop Muon Detectors were brought to the Kamioka Observatory located 1 km underground in the Mozumi Mine, Japan. This mine is home to several high profile experiments, perhaps most notably the 2015 Nobel prize winning particle physics experiment, Super-Kamiokande. Two detectors were placed in the Super-Kamiokande control room for 8 hours, and connected together via a 6-inch 3.5 mm audio cable in configuration (c) of Fig. 6.3. The data was recorded from the coincidence detector through the `import_data.py` script directly to a laptop. Using the same detectors and set-up, a rate measurement was also performed outside the Kamioka mine in the observatory dormitory and in the airplane at 36,000 ft when travelling between Warsaw to Tokyo. Fig. 9.11 shows the trigger rate of the coincident detector for these three measurements, as a function of calculated SiPM peak voltage.

The total number of measured coincident events inside the Super-Kamiokande control room was found to be 101. It was observed that 96% of these events were located below the 50 mV peak described in Sec. ??, indicating that these are likely not minimum ionizing cosmic-ray muons.

The average rock density in the mine was measured to be 2.7 g/cm^3 , corresponding to approximately 2,700 m.w.e. (meter-water equivalent) of overburden [14]. Based on this, we expect the cosmic-ray muon rate to be attenuated by a factor of 10^5 compared to a ground-level measurement. With this assumption, we only expect approximately 0.04 cosmic-ray muon events over

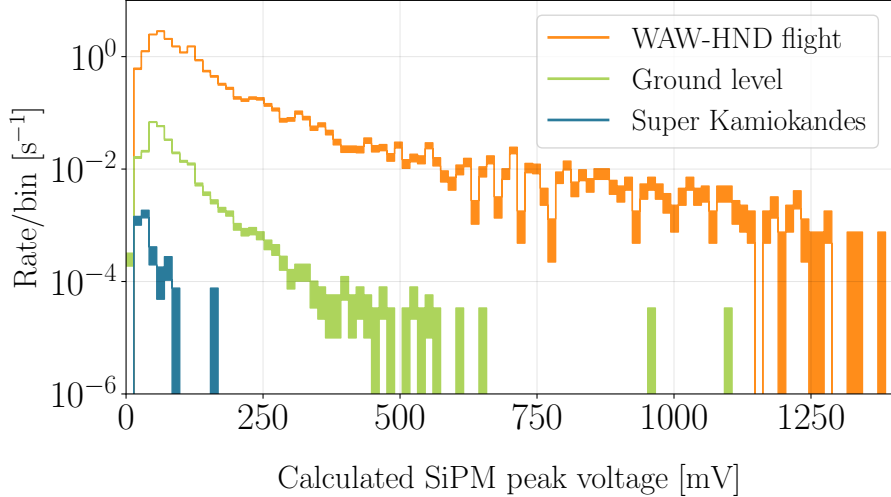


Figure 9.11: The measured coincidence rate at three locations. Data from Ref. [48].

the 8-hour measurement in the Super-Kamiokande control room.

The master detector count rate did not significantly change when it was brought into the mine, indicating that the radioactive background was still present in the control room. Given that the master detector count rate was 1 Hz, Eq. 6.3.1 suggests that we should expect 1-2 accidental coincidence events over the 8-hour period (see Sec. 7).

One unaccounted background (briefly mentioned in Sec. 3.3) consists of events in which a gamma-ray from a radioactive decay Compton scattered off the scintillator of the master detector, and then deposited sufficient energy in the coincident detector scintillator. This is thought to be the dominant source of triggers in this dataset, and a Monte Carlo simulation is currently being developed to investigate this. If these events originate from Compton scattering, we can estimate the rate for these types of events. Given the 101 events (with 1-2 assumed to be accidental coincidences and cosmic-ray muons), the calculated accidental Compton scattering coincidence rate in configuration (c) from Fig. 6.3 is found to be 0.0038 ± 0.0004 . A second 8-hour run was performed using the same configuration and location, which found 92 events (with a similar SiPM peak voltage spectrum) corresponding to a count rate of 0.0035 ± 0.0004 .

This result could be further investigated by repeating the measurement, this time with a thin piece of lead between the scintillator. Lead, being a dense material, is likely to either absorb the gamma-ray or absorb some of the energy from the gamma-ray through Compton scattering. Both processes would reduce the probability of measuring the event with the coincident detector. Another potential source for these events is correlated noise. If the lead does not alter the coincident count rate, this is a potential source for this signal; however, thus far, we have not found any evidence of events due to noise.

9.6 Portable trigger system for an accelerator beamline

This measurement was previously described in Ref. [48] and represents a practical use for the Desktop Muon Detectors.

A single detector, powered by a 10,000 mAh USB power bank, was placed in the Fermilab M-Test facility to trigger on secondary particles (GeV-scale pions and electrons) from the Main Injector. The purpose of this was to trigger a downstream data acquisition system for another experiment. The BNC output at the back of the detector is the raw SiPM pulse, which has a rise time of a few nanoseconds and a decay time of roughly $0.5\ \mu\text{s}$. This signal is useful for experiments that want to use a scintillator but require tens of nanosecond timing. The BNC output was connected to an 80 ft BNC cable to a NIM (Nuclear Instrument Module) rack. The signal passed through a $\times 10$ amplifier and into a discriminator. If the amplified signal was above a certain value, a binary signal was sent to an AND gate, where it was compared against another scintillator paddle trigger that was located on the other side of the other experiment. If the AND condition was satisfied (i.e., the particle passed through both the scintillator paddle and the Desktop Muon Detector), a binary signal was sent to the data acquisition system that began the recording of data of the downstream experiment. Fig. 9.12 shows the trigger rate of the detector placed in the beamline as a function of time. The beam spills occur every minute for two seconds.

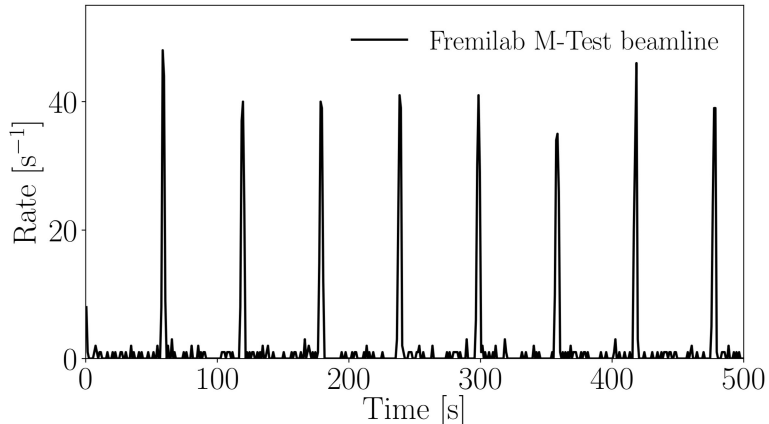


Figure 9.12: The trigger rate as a function of time of a single detector placed in the Fermilab M-Test beamline. Here, the detector is triggering primarily on GeV-scale pions and electrons from the Fermilab Main Injector.

The detector was identified as a useful beamline trigger due to its simplicity. This capability was facilitated by incorporating a BNC output directly connected to the SiPM. For this measurement, the approximate 10 ns uncertainty in the trigger was deemed acceptable. However, if users desire to utilize the FAST output of the SiPM for single nanosecond precision, the SiPM PCB could be modified. We plan on investigating this sometime in the future.

Chapter 10

FUTURE MEASUREMENTS

This section compiles a list of potential future experiments that we intend to perform. After gather and analysing the data, these will be added into Sec. 7.

1. **cosmic-ray muon rate at different floors of a large concrete building:** Large concrete buildings, like FermiLab would be great to measure the floor to floor vertical attenuation.
2. **Special relativity measurement:** A repeat of the measurement that confirmed special relativity by measuring the muon rate on top and at the bottom of a mountain. This can be demonstrated using the altitude data here; however, climbing a mountain would make a good story.
3. **Thin lead measurements.** Thin lead sheets, above the coincidence detectors will actually cause an increase in the count rate. This is due to the muon creating a shower of secondaries, that spread out and are able to trigger the detectors simultaneously. After a few inches of lead, the shower is attenuated.
4. **Clean room background measurement.** Background measurement in clean room at SNO+, also a coincidence measurement.
5. **Measure the Southern Atlantic Anomaly.** This could be performed by flying from Mexico to northern Africa.
6. **Extreme weather events:** Measure muon rate during a low pressure event – like a hurricane.
7. **Solar flare events:** Capture data during an intense solar flare.
8. **Solar activity:** There is an 11-year due to the solar activity that modulates the low-energy cosmic rays.

Chapter 11

CONCLUSION

The CosmicWatch Desktop Muon Detectors offer a versatile platform for exploring diverse natural phenomena. This document provided a comprehensive overview of the underlying physical processes influencing the detectors and demonstrated how valuable insights can be derived from the collected data. The detectors can be employed to investigate a wide range of phenomena related to the geomagnetic field, atmospheric conditions, cosmic-ray shower composition, particle attenuation in matter, radioactivity, and statistical properties of Poisson processes. Students are encouraged to further develop the concepts introduced or design their experiments. Feedback is highly welcomed to enhance and refine this manual. Enjoy your exploration with the CosmicWatch detectors!

Appendix A

Detailed description of the electronics

A.1 The analog circuit

This sub section describes how the analog electronics work. Behind the analog electronics designed to extract information from the SiPM. The amplitude of the SiPM pulse is directly proportional to the energy deposited by the particle that triggered it. Hence, the objective of the analog electronics is to mold the pulse in a way that enables the slow inexpensive micro-controller to measure certain parameters associated with the pulse amplitude.

Fig. A.1 illustrates the four stages of the analog electronics. The SiPM waveform (depicted in red) undergoes an initial amplification of approximately 20x (shown in blue). The amplification signal is then directed into two circuits: a peak detection circuit (green) and a comparator stage which compares the amplified signal to a set trigger threshold voltage level (horizontal dotted line). The peak detector circuit retains the peak value for a sufficient duration, allowing the RP Pico MCU to measure a single value (indicated by the light purple star). The measured ADC value at this point represents the ADC measurement.

Let's break these down.

A.1.1 The amplifier

The SiPM signal is AC coupled to the input of a non-inverting single supply amplifier. After AC coupling with C21, we add a 25 mV voltage bias to the SiPM waveform, to move the waveform away from ground. This is because amplifiers often have trouble amplifying small signals near their power rails. For our amplifier of choice, the TPH2502, the rails are set to V- = GND and V+ = VCC (4.5V). The biased SiPM waveform is sent to the non-inverting input of the first op amp in the TPH2502. The amplification is set through the feedback and gain resistors R5 and

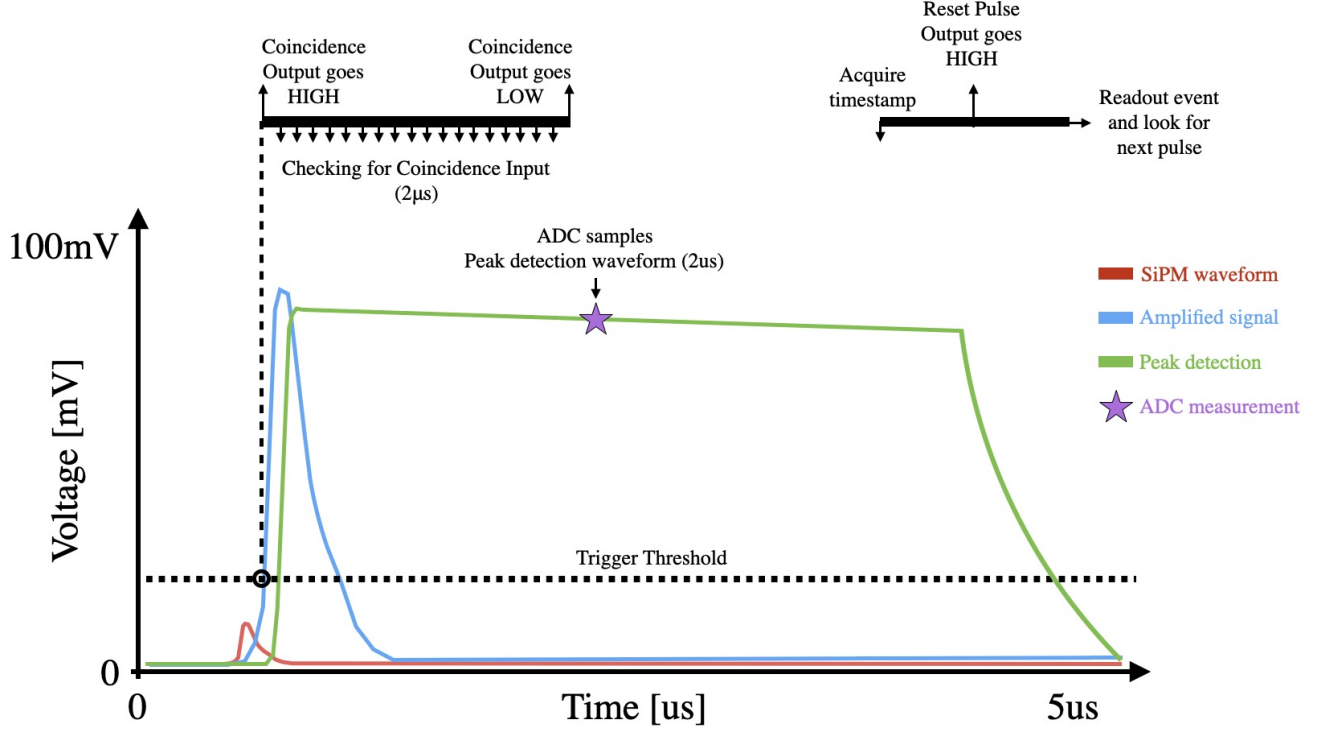


Figure A.1: A description of the analog circuitry and CPU routine. The SiPM pulse (red) is amplified (blue), and peak detected (green). When the amplified pulse crosses the trigger threshold (software defined voltage level), it triggers the detector to 1) check for coincidence signal from coincident detector, 2) samples the amplitude of the peak detector waveform, and 3) takes a time stamp and reads out the event information.

R3, respectively. The gain of the amplifier, to first order is:

$$\frac{V_{out}}{V_{in}} = 1 + \frac{R_F}{R_G} \quad (\text{A.1})$$

In our case, we get a voltage gain of 13.4. Gain is often represented in decibels, which puts it into a logarithmic scale. With this scale, every +6 dB corresponds to doubling the voltage gain. The conversion is:

$$G[\text{dB}] = 20 \log_{10} \left(\frac{V_{out}}{V_{in}} \right) \quad (\text{A.2})$$

Which means our gain also corresponds to 22.6 dB.

The capacitor C22 acts as a high pass filter, that is, it allows high frequencies to pass through, but low frequencies to be blocked. The cutoff for this is around 3 kHz. The amplified pulse is now AC coupled to the second stage of the dual TPH2502 operational amplifier through C18. This is to remove the DC bias that was amplified ($25 \text{ mV} \times 13.4 = 335 \text{ mV}$), as well as the voltage offset introduced through the op amp itself. After removing this offset, we introduce another, well controlled offset, again through the voltage divider setup between R22 and R10, again biasing the waveform by 25 mV. It is this amplified signal that is fed into the peak detector

(second stage of the TPH2502 (U2)), and the comparator circuit. You can look at the amplified pulse using the testpoint TP1.

A.1.2 The peak detector

The peak detector aims to hold peak voltage of the amplifier for sufficient time that we can measure it using the relatively slow RP Pico. The non-inverting input to the peak detector is the 25 mV biased amplified pulse. The output is driven through a diode (D4) to charge a capacitor (C5). The TPH2502 is great at this. It can output quite a large amount of current for its physical size. The inverting input is connected to the charging capacitor. After the pulse subsides, the diode D4 becomes back biased and doesn't conduct. Therefore the charging capacitor can't discharge, and it holds its peak voltage. We then buffer this signal using another TPH2502, that feeds the signal through a voltage divider to match the maximum output from the peak detector given the powering rails, to the ADC dynamic range (0 to 2.5 V). The voltage divider R24 and R27, reduce the peak detector amplitude to about 565% its original size. The peak detector works quite well, and took quite a bit of tuning, both in terms of finding an adequate op amp, as well as optimizing the components. You can look at the amplified pulse using the test point TP2.

After the detector has made its measurement of the peak detector voltage, a digital Trigger Reset command shorts the capacitor C5 through a $1\text{ k}\Omega$ resistor with a MOSFET transistor (Q2).

A.1.3 The comparator

The amplifier also feeds a comparator circuit, the non-inverting input to the second stage of the TPH2502 (U5). When the amplified signal is larger than the inverting input voltage (the trigger threshold), the op amp goes high and outputs a 4.5V pulse, whose length is as long as the amplified pulse stays above the threshold. The trigger threshold, the voltage at which the detector will trigger its readout is set using the pulse width modulation (PWM) of the RP Pico. The voltage is set by a 1 MHz PWM frequency, whose duty cycle is tunable in the configuration file. This digital signal is sent through a voltage divider and low pass filter, setup by R19 and R21, and C11. This makes a pretty nice and clean DC voltage that sets the trigger threshold.

A.2 Digital circuit

The digital side of the circuit consists of the RP Pico, the SD card writer, the temperature and pressure sensor, the OLED screen, the buzzer, the coincidence connector, the LEDs, and

the accelerometer. Eventually, we'll make an expansion module that can connect up to the coincidence connector to introduce additional peripherals.

A.2.1 Raspberry Pi Pico

The Raspberry Pi Pico is a small, low-cost, high-performance microcontroller board built around the RP2040 chip, which was designed in-house by the Raspberry Pi Foundation. Key features:

- Processor: Dual-core ARM Cortex-M0+ at 133 MHz
- Memory: 264 KB of SRAM and 2 MB of onboard Flash storage
- Connectivity: 26 GPIO pins (General Purpose Input/Output). Supports I²C, SPI, UART, PWM, and ADC (analog-to-digital conversion).
- Micro-USB port for programming and communication.
- Power: Runs on 1.8–5.5V (very flexible for projects).
- Programming: You can program it in C/C++ or MicroPython easily. MicroPython is too slow for this project.
- Drag-and-drop programming: when you connect it by USB, it appears like a USB drive — you just drag your code onto it.
- Size: About 21mm × 51mm — tiny, like a stick of gum!

A.2.2 SD card writer

The SD card uses the SPI communication protocol on SPI1 of the RP Pico.

A.2.3 Temperature and pressure sensor

The BMP280 is a high-precision, low-power digital barometric pressure and temperature sensor developed by Bosch Sensortec. It is widely used in applications such as weather monitoring, altitude measurement, indoor navigation, and IoT devices. We talk to it through i2C protocol. Below is a detailed description of its key features, specifications, and functionality:

- I²C address: 0x76 or 0x77 (depending on the SDO pin state).

- Compact Size: Packaged in a small LGA (Land Grid Array) footprint: 2.0 mm x 2.5 mm x 0.95 mm.
- Low Power Consumption: $\sim 2.7 \mu\text{A}$ at 1 Hz sampling rate.
- Pressure Resolution: 0.16 Pa
- Temperature Resolution: 0.01°C
- Absolute Accuracy: Pressure: $\pm 10 \text{ hPa}$ (typical). Temperature: $\pm 3^\circ\text{C}$ (typical).

Appendix B

The Firmware

At the top of Fig. A.1, an approximation of the routine executed by the CPU is presented. When the amplified signal triggers the detector readout, we immediately send out the coincidence output signal and search for a coincidence input signal. We ask whether the coincidence input is HIGH 32 times (each ask takes 72 ns) and if any of them are true, the event is counted as a coincident event. After determining if the event was coincident, the ADC samples the peak detector waveform. A single ADC sample takes approximately $2\mu\text{s}$. We then set the coincidence output to LOW, acquire the timestamp of the event, and reset the peak detector, and populates the variables that hold the event information. Finally, we print the event information to the serial port and flash the LEDs appropriately. The above all happens on the first core of the RP Pico.

The second core runs continuously in a while loop. The loop sequentially updates the OLED screen, then reads

Fig. B.1 displays the printed circuit boards (PCBs) utilized in the v3 detector. The left (right) side showcases the bottom (top) of the PCBs. The PCB comprises two distinct pieces: the SiPM PCB and the Main PCB. Each component of the circuitry is appropriately labeled. The blue box denotes the analog circuitry, as described previously, while the purple box represents power handling. This includes a DC-DC booster that elevates the 5V voltage from the USB connection to 28.9V and a 3.6V regulator to supply power to the op amps used in the analog circuitry.

Fig. ?? is provided to illustrate the internal components of the detector. In certain cases, it is preferable to measure the full-sky muon rate. This is most effectively achieved by situating the scintillators between two detectors as closely as possible, as depicted in Fig. 6.3 (d). If your measurement aligns with this configuration, you may choose to remove the detectors from their cases.

The last figure in this section, Fig. ??, presents a vector image of the complete circuit. If you

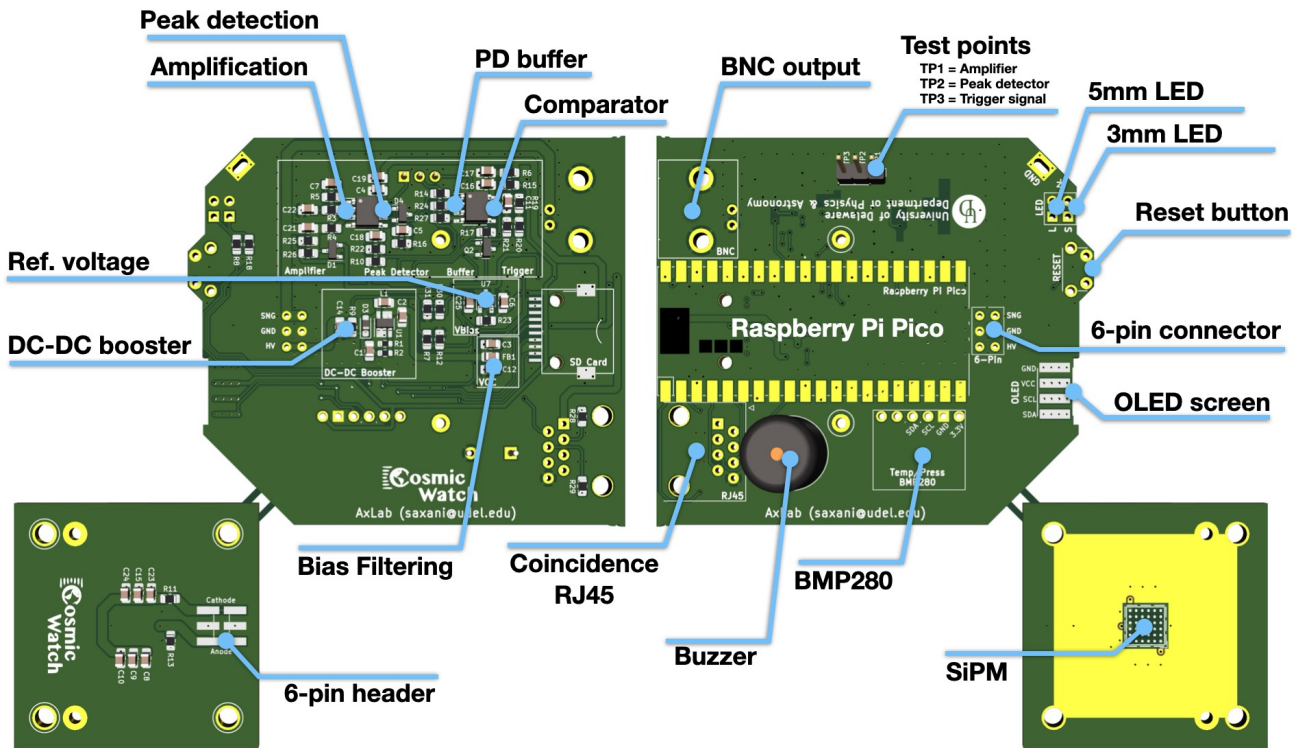


Figure B.1

have any questions, please feel free to reach out to Spencer at saxani@mit.edu, as we will forgo a detailed description here.

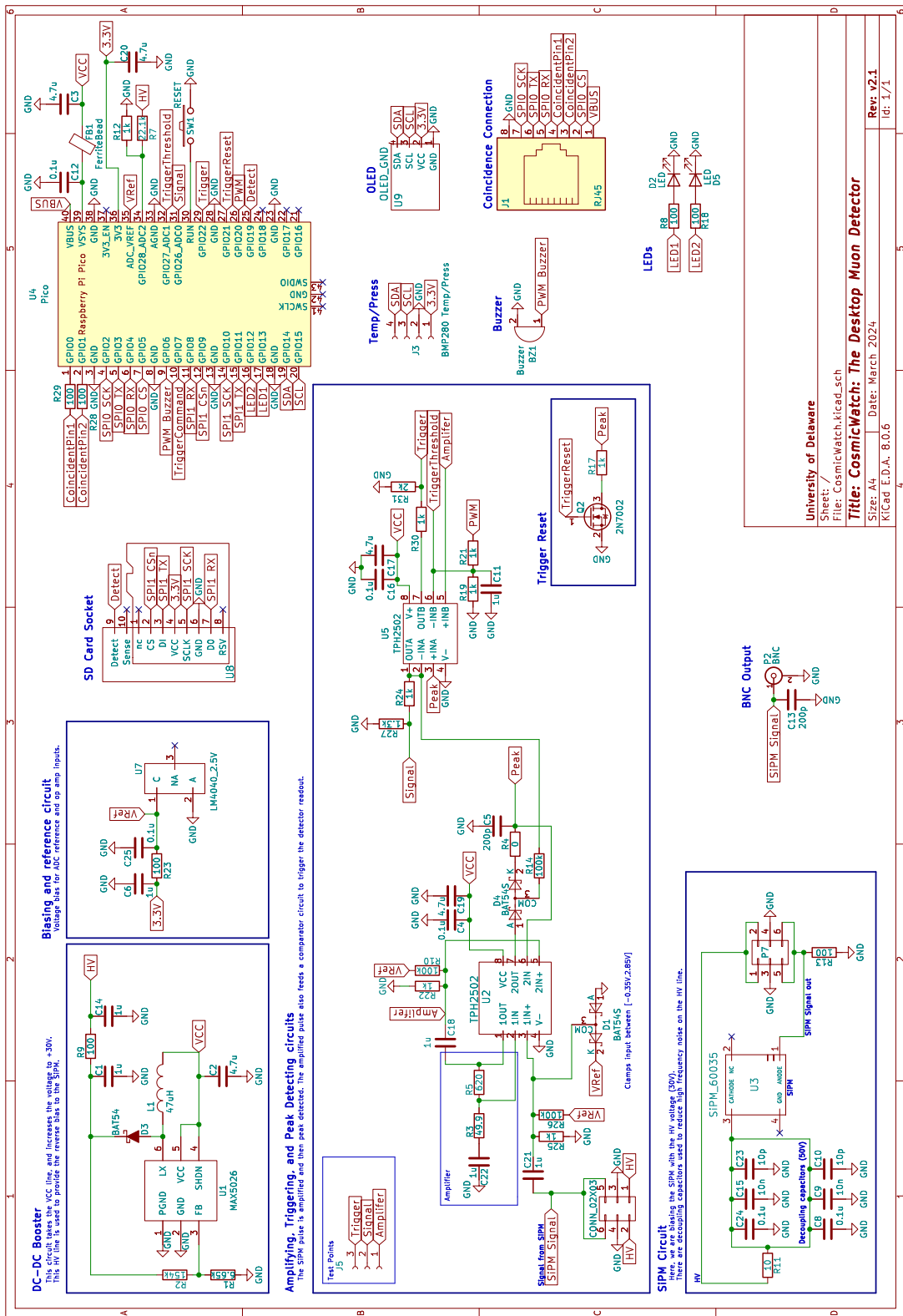


Figure B.2: The circuit diagram of the v3X Desktop Muon Detector. Vectorized version available on GitHub.

Bibliography

- [1] K. O. et al, “Cosmic rays - particle data group,” *Nuclear Instruments and Methods in Physics Research Section A: Accelerators, Spectrometers, Detectors and Associated Equipment*, vol. 38, no. 090001, p. 6, 2014.
- [2] S. K. LBNL, “32. passage of particles through matter,” 2017.
- [3] B. Rossi, “Cosmic rays,” 1964.
- [4] M. W. Friedlander, *A thin cosmic rain: Particles from outer space*. Harvard University Press, 2002.
- [5] P. K. Grieder, *Cosmic rays at Earth*. Elsevier, 2001.
- [6] T. K. Gaisser, R. Engel, and E. Resconi, *Cosmic rays and particle physics*. Cambridge University Press, 2016.
- [7] W. R. Leo, *Techniques for nuclear and particle physics experiments: a how-to approach*. Springer Science & Business Media, 2012.
- [8] C. Grupen and B. Shwartz, *Particle detectors*, vol. 26. Cambridge university press, 2008.
- [9] H. Kolanoski and N. Wermes, *Particle detectors: fundamentals and applications*. Oxford University Press, 2020.
- [10] D. Bird, S. Corbató, H. Dai, B. Dawson, J. Elbert, T. Gaisser, K. Green, M. Huang, D. Kieda, S. Ko, *et al.*, “Evidence for correlated changes in the spectrum and composition of cosmic rays at extremely high energies,” *Physical review letters*, vol. 71, no. 21, p. 3401, 1993.
- [11] G. Taubes, “Pattern emerges in cosmic ray mystery,” *Science*, vol. 262, no. 5140, pp. 1649–1650, 1993.
- [12] F. Halzen and A. D. Martin, “Quarks and leptons,” 1984.
- [13] D. Griffiths, *Introduction to elementary particles*. John Wiley & Sons, 2008.
- [14] M. Fukugita and T. Yanagida, *Physics of Neutrinos: and Application to Astrophysics*. Springer Science & Business Media, 2013.

- [15] M. Tanabashi, P. Richardson, A. Bettini, A. Vogt, L. Garren, A. J. Schwartz, K. Terashi, M. Karliner, R. S. Chivukula, T. Sjöstrand, *et al.*, “Aps: Review of particle physics,” *Phys. Rev. D*, vol. 98, p. 030001, 2018.
- [16] T. K. Gaisser and M. Honda, “Flux of atmospheric neutrinos,” *Annual Review of Nuclear and Particle Science*, vol. 52, no. 1, pp. 153–199, 2002.
- [17] E. Regener and G. Pfotzer, “Vertical intensity of cosmic rays by threefold coincidences in the stratosphere,” *Nature*, vol. 136, no. 3444, p. 718, 1935.
- [18] O. Allkofer, R. Andresen, and W. Dau, “The muon spectra near the geomagnetic equator,” *Canadian Journal of Physics*, vol. 46, no. 10, pp. S301–S305, 1968.
- [19] O. Allkofer, R. Andresen, K. Clausen, and W. Dau, “Sea-level muon spectrum at two different latitudes,” *Journal of Geophysical Research*, vol. 77, no. 22, pp. 4251–4253, 1972.
- [20] C. Augusto, C. Navia, and K. Tsui, “Muon enhancements at sea level in association with swift-bat and milagro triggers,” *Physical Review D*, vol. 77, no. 12, p. 123008, 2008.
- [21] https://www.nasa.gov/mission_pages/station/research/experiments/1043.html, “International space station internal radiation monitoring (iss internal radiation monitoring) - 04.05.17,” Dec 2018.
- [22] T. Dachev, W. Atwell, E. Semones, B. Tomov, and B. Reddell, “Observations of the saa radiation distribution by liulin-e094 instrument on iss,” *Advances in Space Research*, vol. 37, no. 9, pp. 1672–1677, 2006.
- [23] L. Pinsky, W. Osborne, J. Bailey, R. Benson, and L. Thompson, “Light flashes observed by astronauts on apollo 11 through apollo 17,” *Science*, vol. 183, no. 4128, pp. 957–959, 1974.
- [24] C. Fuglesang, L. Narici, P. Picozza, and W. G. Sannita, “Phosphenes in low earth orbit: survey responses from 59 astronauts,” *Aviation, space, and environmental medicine*, vol. 77, no. 4, pp. 449–452, 2006.
- [25] A. Rinaldi, “Phosphenes in space: a study on the interaction between carbon ions and rod photoreceptor,” 2009.
- [26] C. Augusto, C. Navia, H. Shigueoka, K. Tsui, and A. Fauth, “Muon excess at sea level from solar flares in association with the fermi gbm spacecraft detector,” *Physical Review D*, vol. 84, no. 4, p. 042002, 2011.
- [27] M. Savić, D. Maletić, D. Joković, N. Veselinović, R. Banjanac, V. Udovičić, and A. Dragić, “Pressure and temperature effect corrections of atmospheric muon data in the belgrade cosmic-ray station,” in *Journal of Physics: Conference Series*, vol. 632, p. 012059, IOP Publishing, 2015.
- [28] P. H. Barrett, L. M. Bollinger, G. Cocconi, Y. Eisenberg, and K. Greisen, “Interpretation of cosmic-ray measurements far underground,” *Reviews of Modern Physics*, vol. 24, no. 3, p. 133, 1952.

- [29] F. An, A. Balantekin, H. Band, M. Bishai, S. Blyth, D. Cao, G. Cao, J. Cao, Y. Chan, J. Chang, *et al.*, “Seasonal variation of the underground cosmic muon flux observed at daya bay,” *Journal of Cosmology and Astroparticle Physics*, vol. 2018, no. 01, p. 001, 2018.
- [30] A. Bouchta, “Seasonal variation of the muon flux seen by amanda,” in *International Cosmic Ray Conference*, vol. 2, p. 108, 1999.
- [31] M. Ambrosio, R. Antolini, G. Auriemma, R. Baker, A. Baldini, G. Barbarino, B. Barish, G. Battistoni, R. Bellotti, C. Bemporad, *et al.*, “Seasonal variations in the underground muon intensity as seen by macro,” *Astroparticle Physics*, vol. 7, no. 1-2, pp. 109–124, 1997.
- [32] W. Benenson, J. W. Harris, H. Stöcker, and H. Lutz, *Handbook of physics*. Springer Science & Business Media, 2006.
- [33] D. Green, *The physics of particle detectors*, vol. 12. Cambridge University Press, 2000.
- [34] W. Li, M. D. Rodriguez, P. Kluth, M. Lang, N. Medvedev, M. Sorokin, J. Zhang, B. Afra, M. Bender, D. Severin, *et al.*, “Nu clear instrum ents and methods in phy sics research b,” *Nuclear Instruments and Methods in Physics Research B*, vol. 302, pp. 40–47, 2013.
- [35] K. A. Olive *et al.*, “Review of Particle Physics,” *Chin. Phys.*, vol. C38, p. 090001, 2014.
- [36] B. R. Martin, *Nuclear and particle physics: an introduction*. John Wiley & Sons, 2006.
- [37] T. Tabata, R. Ito, and S. Okabe, “An empirical equation for the backscattering coefficient of electrons,” *Nuclear instruments and methods*, vol. 94, no. 3, pp. 509–513, 1971.
- [38] M. J. Berger and S. M. Seltzer, “Stopping powers and ranges of electrons and positions,” tech. rep., NATIONAL STANDARD REFERENCE DATA SYSTEM, 1982.
- [39] https://www.onsemi.com/pub/Collateral/AND9770_D.PDF, “On semiconductor: Introduction to the silicon photomultiplier,” Dec 2018.
- [40] <https://www.sensl.com/downloads/ds/TN>
- [41] A. Pla-Dalmau, A. D. Bross, V. V. Rykalin, and B. M. Wood, “Extruded plastic scintillator for minerva,” in *Nuclear Science Symposium Conference Record, 2005 IEEE*, vol. 3, pp. 1298–1300, IEEE, 2005.
- [42] Eljen. <https://eljentechnology.com/products/plastic-scintillators>, accessed: Oct 2018 2018.
- [43] H. Yang, D. Cao, Z. Qian, X. Zhu, C. Loh, A. Huang, R. Zhang, Y. Yang, Y. Liu, B. Xu, *et al.*, “Light attenuation length of high quality linear alkyl benzene as liquid scintillator solvent for the juno experiment,” *Journal of Instrumentation*, vol. 12, no. 11, p. T11004, 2017.
- [44] D. Beznosko, A. Bross, A. Dyshkant, and P.-D. Rykalin, “Fnal-nicadd extruded scintillator,” in *Nuclear Science Symposium Conference Record, 2004 IEEE*, vol. 2, pp. 790–793, IEEE, 2004.

- [45] D. Horrocks, *Applications of liquid scintillation counting*. Elsevier, 2012.
- [46] I. Ambats, Y. Antipov, A. Sadovski, K. Lang, W. Allison, D. Wall, A. Napier, Y. Lai, R. Heinz, D. Wright, *et al.*, “The minos detectors technical design report,” tech. rep., 1998.
- [47] L. Aliaga, L. Bagby, B. Baldin, A. Baumbaugh, A. Bodek, R. Bradford, W. Brooks, D. Boehnlein, S. Boyd, H. Budd, *et al.*, “Design, calibration, and performance of the minerva detector,” *Nuclear Instruments and Methods in Physics Research Section A: Accelerators, Spectrometers, Detectors and Associated Equipment*, vol. 743, pp. 130–159, 2014.
- [48] S. N. Axani, K. Frankiewicz, and J. M. Conrad, “The cosmicwatch desktop muon detector: a self-contained, pocket sized particle detector,” *Journal of Instrumentation*, vol. 13, no. 03, p. P03019, 2018.
- [49] R. De Mendonca, J.-P. Raulin, E. Echer, V. Makhmutov, and G. Fernandez, “Analysis of atmospheric pressure and temperature effects on cosmic ray measurements,” *Journal of Geophysical Research: Space Physics*, vol. 118, no. 4, pp. 1403–1409, 2013.
- [50] LocalConditions.com. <https://www.localconditions.com/weather-madison-wisconsin/53701/past.php>, accessed: Dec. 2018.
- [51] K. Jourde, D. Gibert, J. Marteau, J. de Bremond d’Ars, S. Gardien, C. Girerd, and J.-C. Ianigro, “Monitoring temporal opacity fluctuations of large structures with muon radiography: a calibration experiment using a water tower,” *Scientific reports*, vol. 6, p. 23054, 2016.
- [52] Flight Aware. <https://flightaware.com/>, Dec. 2017.
- [53] <http://nearspace.pl/>, “Near space conference 2018,” Dec 2018.
- [54] K. Albrecht *et al.* (The IceCube Collaboration), “IceCube - the next generation neutrino telescope at the South Pole,” *Nuclear Physics B-Proceedings Supplements*, vol. 118, pp. 388–395, 2003.